AIChE WILEY InterScience DISCOVER SOMETHING GREAT

PARTICLE TECHNOLOGY AND FLUIDIZATION

Fluidization of Fine and Ultrafine Particles Using Nitrogen and Neon as Fluidizing Gases

Jose Manuel Valverde, M. A. S. Quintanilla, and Antonio Castellanos
Faculty of Physics, Universidad de Sevilla, Avenida Reina Mercedes s/n, 41012 Sevilla, Spain

Daniel Lepek, Jose Quevedo, Rajesh N. Dave, and Robert Pfeffer
New Jersey Center for Engineered Particulates, New Jersey Institute of Technology, Newark, NJ 07102

DOI 10.1002/aic.11329
Published online November 9, 2007 in Wiley InterScience (www.interscience.wiley.com).

When fluidized by a gas, some agglomerated fine and ultrafine particles display a regime of uniform, nonbubbling fluidization known as agglomerate particulate fluidization (APF). The agglomeration of micrometric sized particles, or simple pre-existing agglomerates in the case of nanoparticles, is governed by the balance between hydrodynamic shear forces and interparticle attractive forces. From this balance the theoretical scaling law $\mathrm{Bo_g} \sim \mathrm{k}^{D+2}$ *has been derived, where* $\mathrm{Bo_g}$*, the granular Bond number, is the ratio of the interparticle attractive force to particle weight,* k *is the ratio of agglomerate to particle size, and* D *is the fractal dimension. In the experimental program the behavior of gas-fluidized beds of fine and ultrafine particles as affected by the use of neon and nitrogen as fluidizing gas is studied. The experimental results indicate that there is no relevant distinction between the sizes of agglomerates fluidized with the different gases as theoretically predicted. However, it is seen that the relatively small increment of gas viscosity opens up a new window of highly expanded agglomerate particulate fluidization (APF) behavior with a delayed onset of bubbling. For a sufficiently high-gas viscosity, and/or smaller particle size, full suppression of the bubbling regime is observed. For nanoparticles exhibiting agglomerate bubbling fluidization (ABF) behavior, where bed expansion is small, and bubbling occurs soon after minimum fluidization, we also observe a delayed onset of bubbling when fluidizing with a gas of higher viscosity*. © 2007 American Institute of Chemical Engineers *AIChE J,* 54: 86–103, 2008
Keywords: fluidization, bubbling, fine particles, nanoparticles, agglomeration

Introduction

Fine powders are receiving an increased interest in industry and academia due to their novel physical, chemical and mechanical properties. Gas-phase processes are often employed in the production of fine particles and gas-fluidized beds of fine particles are usually found in applications where solid-gas reaction efficiency needs to be improved. For example, flame aerosol reactors[1] have been employed in industry for several decades to manufacture nanoparticles of carbon black, silica, alumina, and titania by using the flame heat to initiate chemical reactions producing condensable monomers. In these production processes the extremely high-temperatures that are needed may significantly alter the gas properties relevant for the solid-gas interaction, such as gas viscosity. It is well known that fluid viscosity has a fundamental role on the fluidization dynamics since the fluid drag acting on particles in a dense suspension affects the formation

Correspondence concerning this article should be addressed to J. M. Valverde at jmillan@us.es.

of flow structures. Usually fluidized beds are unstable and contain flow heterogeneities, such as fluid bubbles which arise throughout the bed and curtail uniform expansion. The question on the origin of bubbles, and the distinction between nonbubbling uniform fluidization and bubbling heterogeneous fluidization is one of the fundamental problems that, even for noncohesive particles, still raises strong concerns. Needless to say a quantitative theory to predict the behavior of fluidized beds of fine cohesive particles as affected by gas viscosity and interparticle attractive forces does not exist.

The rest of the introduction is devoted to a brief summary on the types of fluidization behavior observed for fluidized beds of noncohesive particles, and the empirical criteria formulated for their prediction. In the next sections, we make some theoretical considerations on the behavior of fluidized beds of fine cohesive particles that would lead us to predict a variety of flow behaviors. Finally, we show experimental data on fluidized beds of micrometric and nanometric sized particles. Experimental results will be discussed on the basis of our theoretical analysis. A main conclusion of our work is that high-viscosity gas, and/or ultrafine particle fluidization may lead to a full suppression of the bubbling regime in gas-fluidized beds as seen in liquid-fluidized beds of noncohesive particles.

On the empirical criteria to predict uniform fluidization in fluidized beds of noncohesive particles

A relevant parameter that characterizes the cohesiveness of a granular material is the granular Bond number Bo_g, defined as the ratio of interparticle attractive force F_0 to particle weight W_p. Typically particles of size $d_p \gtrsim 50\mu$m exhibit a free-flowing behavior, whereas smaller particles, for which $Bo_g > 1$, show a tendency to aggregate that inhibits powder flow.[2]

As far as fluidization of noncohesive particles concerns, the pioneer work by Wilhelm and Kwauk[3] differentiated the behavior of liquid-fluidized beds, which exhibited the so-called particulate fluidization, from that of gas-fluidized beds, which bubbled just beyond the point at which their yield strength vanished. They delineated the transition between uniform and bubbling fluidization, based on an empirical Froude number (Fr) criterion that stated

$$Fr = \frac{v_{mf}^2}{g d_p} \gtrsim 1 \tag{1}$$

for bubbling behavior, where v_{mf} is the superficial gas velocity taken at the fluidizing point and g is the gravity acceleration. This separation between gas-fluidized and liquid-fluidized beds has persisted for many years in spite of the fact that Wilhelm and Kwauk already reported the appearance of bubbling for liquid-fluidized lead spheres, and predicted that very fine powders might attain particulate fluidization by virtue of small gas velocities.

In order to estimate the largest stable size D_b of isolated fluid bubbles, Harrison et al.[5] working on fluidized beds of noncohesive particles, hypothesized that bubbles are no longer stable if their rising velocity U_b exceeds the terminal settling velocity of an individual particle v_{p0}. In the small Reynolds number regime $v_{p0} \simeq (1/18)(\rho_p - \rho_f) d_p^2 g/\mu$, where ρ_p is the particle density, ρ_f is the fluid density, and μ is the fluid viscosity. Using the semiempirical relation $U_b \simeq 0.7\sqrt{gD_b}$,[6,7] we have

$$\frac{D_b}{d_p} \simeq \frac{1}{18^2\, 0.7^2} \frac{(\rho_p - \rho_f)^2 g\, d_p^3}{\mu^2} \tag{2}$$

Harrison et al. carried out an extensive series of experimental observations on fluidized beds with varying μ, ρ_p and ρ_f, and concluded that the ratio D_b/d_p coincided with bubbling behavior when $D_b/d_p \gtrsim 10$, and with uniform fluidization when $D_b/d_p \lesssim 1$. For example, lead shot particles could be uniformly fluidized by a 75 wt% aqueous solution of glycerol ($D_b/d_p = 1.9$), but experienced bubbling using pure water ($D_b/d_p = 14.8$). In the range described approximately by $1 \lesssim D_b \lesssim 10$, the fluidized beds showed a transition from nonbubbling to bubbling behavior. Interestingly, Harrison et al. reported on experiments of beds of light phenolic microballoons ($\rho_p \simeq 240$ kg/m^3, $d_p \simeq 125$ μm); fluidized with CO_2 at various pressures, which showed bubbling behavior at ambient pressure ($D_b/d_p \simeq 24$), but nonbubbling fluidlike behavior at high-gas pressures ($D_b/d_p \simeq 2$), against the common belief that gas-fluidized beds do always bubble. Harrison et al. tried to justify their hypothesis by postulating that the gas velocity through a bubble, and relative to it, is of the same magnitude as U_b. Thus, in the limit $U_b = v_{p0}$, particles from the wake carried up to the interior by circulating fluid would destroy the bubble. However, examples of bubble breakup by instability of its roof were later found[8,9] that devalued the relevance of this pioneer work in spite of the empirical evidence. Unfortunately, theoretical studies on bubble roof stability, considering the upper interface bubble-dense phase as an interface undergoing a Rayleigh-Taylor instability,[10] fail to predict a quantitative limit value for D_b, that could be compared to experimental results.[9,11] However, the distinction between bubble breakup from the roof and from the wake is blurred because of the gas throughflow associated with bubble interaction during or following coalescence.[7] Thus, even though the Harrison et al. criterion can be useful for an estimation of the fluidization homogeneity, the collective interaction between bubbles through splitting-coalescence mechanism can ultimately lead to equilibrium bubble sizes larger than Harrison's maximum stable size as seen in experiments.[12] Note, however, that the Harrison criterion conforms to the Wilhelm & Kwauk empirical criterion (Eq. 1) if the Froude number is defined based on the terminal settling velocity of an individual particle ($Fr_0 = v_{p0}^2/(gd_p)$).

The general theory proposed by Wallis[13] to describe a large class of dynamic systems, such as sound waves in a gas or traffic flow, has also been employed in order to predict the transition to bubbling behavior. Following the Wallis theory, some authors[14] have suggested that bubbles in fluidized beds are an outcome of the formation of concentration shocks or discontinuities in particle concentration, when the propagation velocity of a voidage disturbance (u_ϕ) surpasses the elastic wave velocity (u_e) of the bed. It is well accepted that u_ϕ can be obtained from the relation $u_\phi = -\phi dv_g/d\phi$, where ϕ is the particle volume fraction, and v_g is related to ϕ by the Richardson-Zaki empirical equation

$$v_g = v_{p0}(1-\phi)^n \tag{3}$$

where $n \simeq 5.6$ in the small Reynolds number limit.[15] On the other hand, the elastic wave velocity u_e is given by $u_e = [(1/\rho_p)\ (\partial p/\partial\phi)]^{1/2}$, where p is the particle-phase pressure, which is defined from the trace of the particle-phase stress tensor. The existence of multiple contributing sources to the particle-phase pressure, and the lack of experimental evidence have led researchers to propose different mechanisms for predicting the particle-phase pressure that have provoked sharp controversies.[11] One component of the stress should appear as a result of the momentum transfer due to the fluctuating velocity of the particle phase. Another main component stems from the momentum transfer between particles during collisions. Sometimes a hydrodynamic contribution to the particle stress tensor is added to account for the drag. Particle-phase stresses can also appear due to the possible solid-like behavior of the bed, because of enduring interparticle contacts at high-particle concentrations.[16] Usually it is assumed that the particle-phase pressure is a simple function of the particle volume fraction $p(\phi)$. In spite of the uncertainty on the dependence of p on ϕ, it seems reasonable that the particle-phase pressure in the expanded fluidized bed increases with ϕ for small ϕ.[16] Measurements of the collisional pressure in a water-fluidized bed by Zenit et al.[17] could be well-fitted to the equation $p \sim \rho_p g d_p \phi^2$ in the range $\phi \lesssim 0.3$. A recent numerical study predicts an analogous variation of the granular pressure.[18] A similar relationship was also derived by Foscolo and Gibilaro (hereafter F-G), who neglected particle inertia, and related p to the fluid-particle drag force in an ideal homogeneous state.[19] Foscolo and Gibilaro used the Wallis criterion to predict the onset of bubbling in fluidized beds, however, Batchelor[14] and Jackson[11] pointed out that the F-G derivation of $p(\phi)$ was conceptually wrong since the pressure variation cannot be due only to a dissipative process, but also by momentum transport due to particle fluctuations and collisions that must be necessarily considered. In spite of this, it is undeniable that Foscolo and Gibilaro found good agreement with observations on the initiation of visible bubbling in liquid and gas-fluidized beds at both laminar and turbulent conditions.[19] Additionally, the F-G criterion was successfully applied by other authors under systematic variations of relevant parameters on the bubbling point of gas-fluidized beds, such as pressure, temperature and addition of fines.[20] Using $p \sim \rho_p g d_p \phi^2$, the Wallis criterion applied to the bubbling onset in fluidized beds of noncohesive particles can be summarized as

$$\begin{aligned} &u_\phi \simeq \phi \frac{1}{18}\frac{(\rho_p - \rho_f)\ d_p^2\ g}{\mu}\ n\ (1-\phi)^{n-1} \\ &u_e \simeq (g\, d_p\, \phi)^{1/2} \\ &u_\phi < u_e \text{ nonbubbling regime} \\ &u_\phi \simeq u_e \text{ at bubbling onset} \end{aligned} \tag{4}$$

Despite the apparent success of Eq. 4 in discriminating between systems observed to bubble and those that do not, it must be made clear that this criterion is theoretically based on the assumption that nonbubbling beds are necessarily stable (see Ref. 11 for a detailed discussion). In a numerical analysis, Glasser, Kevrekidis and Sundaresan[21] have examined the evolution of traveling wave solutions through direct numerical integration of the volume-averaged equations. In this analysis, the particle-phase pressure and viscosity were assumed to be monotonically increasing functions of the particle volume fraction. It was clearly demonstrated that the distinction between bubbling and nonbubbling systems was linked with high-amplitude solutions as seen in liquid-fluidized beds, in which small bubbles that do not develop into large visible bubbles have been observed.[9,11] Glasser et al.[21] carried out a limited parametric study and concluded that the parameter

$$\Omega = \left(\frac{\rho_p\, v_{p0}^3}{\mu_s\, g}\right)^{1/2} \tag{5}$$

determined whether large amplitude bubbles evolved from the initial value problem. Here μ_s is a measure of the particle-phase viscosity. Glasser et al. made the rough assumption that the scale for the particle-phase viscosity is inertial rather than viscous, leading to $\mu_s \sim \rho_p v_{p0} d_p$. In his review on the origin of bubbles, Homsy[22] qualifies this assumption as "a leap of faith—albeit a provocative one—until more is known about the rheology of the fluidized state". Note that, with this assumption, Ω^2 turns out to be just the Froude number. Thus, the differentiation between bubbling and uniform fluidization was expressed in terms of a Froude number criterion also from this numerical study on the transient development of large-amplitude nonlinear solutions.

Using Eq. 2 in Eq. 4 it can be shown that

$$\frac{u_e - u_\phi}{u_e} = 1 - 0.7n\left(\frac{D_b}{d_p}\right)^{1/2}\phi^{1/2}(1-\phi)^{n-1} \tag{6}$$

Since the function $f(\phi) = \phi^{1/2}\ (1-\phi)^{n-1}$ takes a maximum value of $f(\phi) \simeq 0.2$ at $\phi \simeq 0.1$, we have that $\min(u_e - u_\phi) \gtrsim 0$ for $D_b/d_p \lesssim 1$. Thus, for $D_b/d_p \lesssim 1$ it is $u_e \gtrsim u_\phi\ \forall\phi > 0$, i.e., the nonbubbling behavior predicted by the Harrison criterion coincides with the absence of a transition to bubbling according to the Wallis criterion. On the other hand, for $D_b/d_p \gtrsim 1$ both criteria agree in predicting a transition to bubbling. This correlation between the Harrison and Wallis criteria was already noted in Ref. 23.

The Froude number and Harrison criteria are unable to predict the particle volume fraction at the onset of bubbling for fluidized systems exhibiting a transition from uniform to bubbling fluidization. It will be shown that small bubbles can also be identified also in our fine powders fluidized by gas in a regime of uniform fluidization previous to the onset of large bubbles. In a recent review, Sundaresan[16] discusses this problem and recognizes that, in contrast with the commonly encountered case of gas-fluidized beds stabilized by yield stresses associated with enduring particle networks, the hydrodynamic mechanism that restrains bubbling in gas-fluidized beds of fine powders remains to be explained. However, it must be commented that according to empirical observations,[9,11,22] uniform fluidized beds in a fluid-like regime are not necessarily stable, which leaves the Wallis criterion (Eq. 4) without a well-founded physical justification. Despite the absence of a physical basis for Eq. 4, we will use it in this work just as an empirical equation to predict the particle volume fraction at the onset of large amplitude bubbling phenomenon in our fluidized beds.

Empirical Criteria to Predict Uniform Fluidization in Fluidized Beds of Cohesive Particles

Fine and ultrafine powders have been traditionally classified as Group C materials according to Geldart's classification scheme,[24] and, thus, theoretically, they are not capable of being fluidized because interparticle forces are exceedingly large as compared to particle weight. Consequently, Group C powders tend to rise as a slug of solids or to form channels through which the fluid will escape rather than being distributed through the bulk. Typical examples are talc, flour and starch. This type of behavior contrasts with the behavior of aeratable Geldart A powders (of particle size between $\sim$20 μm and $\sim$200 μm for typical particle densities $\rho_p \sim$ 1,000 kg/m^3) that exhibit uniform fluidization for an interval of gas velocities between the minimum fluidization velocity and the minimum gas velocity for the bubbling onset.[24] The question on the source of stability of fluidized beds of Geldart A powders has been a subject of controversy for many years. Most of the experimental results suggest that in the uniform fluidization state the bed behaves like a weak solid rather than a fluid due to enduring interparticle contacts caused by interparticle cohesive forces.[25] Notable exceptions include examples of gas-fluidization of light particles, showing a fluid-like behavior reminiscent of liquid-fluidized beds. This type of smooth fluid-like fluidization was already reported in 1961 by Harrison et al.[5] for light phenolic microballoons fluidized with CO_2 at high-pressures. Richardson[26] also reported bubble-free fluidization for fine powders of low-solid density, with a ratio of minimum bubbling to minimum fluidization gas velocities of up to 7.5.

The enormous relevance of the fluidization properties of Geldart A powders for industrial applications has long been recognized in chemical engineering fields. However, industry requirements of using particles having a higher ratio of surface area to volume to provide enhanced fluid-solid contact and reaction efficiencies have led researchers to focus on gas-fluidization of particles smaller than $\sim$20 μm. As a result it has been discovered that, in spite of the predicted Geldart C behavior, it is possible to uniformly fluidize micron and submicron-sized particles in a fluid-like regime. Reports of uniform fluidization of micron and submicron primary particles can be found from the middle 1980s.[27–30] A common observation was that uniform fluidization was closely related to the formation of light agglomerates when fluidizing the original powder at a superficial gas velocity much larger than the expected minimum fluidization velocity for the system of individual primary particles. Chaouki et al.[27] made a distinction between Geldart C powders, and a separate smaller class, C′, described as "a typical clustering powder", that fluidized via self-agglomeration of the primary particles, thus, behaving as a system of low-density fluidizable particles. Since the condition of non-bubbling fluid-like fluidization is linked to the formation of porous light agglomerates, this type of fluidization has been recently termed as agglomerate particulate fluidization (APF).

Fluidization of fine particles

Some of the works showing uniform fluidization of fine and ultrafine powders use aids in order to help fluidization. One of these fluidization aids consists of coating micron sized particles with surface additives that decrease interparticle cohesion.[31,32]

Since the suppression of gas bubbles is related to the existence of porous light agglomerates, a relevant property is the size of the agglomerate. Fine particles agglomerate in the fluidized bed driven by the dynamic equilibrium between the interparticle attractive force F_0 and the flow shear, which supports the particle weight in the gravity field. Assuming that the maximum shear force that each agglomerated particle can stand is of the order of the interparticle attractive force F_0, the scaling law

$$Bo_g \sim N k^2 = k^{D+2} \tag{7}$$

has been derived to estimate the agglomerate size d^*.[33] Here N is the number of particles agglomerated, k is the ratio of d^* to particle size d_p, and we have used the fractal dimension of the agglomerate ($D = \ln N/\ln k$). In order to consider gas flow screening by the agglomerates, it is assumed that agglomerates are approximately spherical and that the agglomerate hydrodynamic radius can be approximated to its gyration radius. As estimated by Zhu et al.,[34] the error in assuming that highly porous nanoparticle agglomerates behave as solid particles for the purposes of hydrodynamic analysis is small. Also, if a monodisperse distribution of agglomerates is assumed, the settling velocity of the fluidized bed v_s can be described by the modified R-Z law (see Ref. 35 for a detailed derivation)

$$\frac{v_s}{v^*} = (1 - \phi^*)^n \tag{8}$$

where $v^* = v_{p0}\, N/k$ is the terminal settling velocity of an individual agglomerate (hereafter, we neglect gas density ρ_f as compared to agglomerate density $\rho^* = \rho_p\, N/k^3$), and $\phi^* = \phi\, k^3/N$ is the volume fraction of the agglomerates in the fluidized bed. Thus, Eq. 8 may be rewritten as

$$\frac{v_s}{v_{p0}} = \frac{N}{k}\left(1 - \frac{k^3}{N}\phi\right)^n \tag{9}$$

Settling experiments[36] performed on fine powders with varying particle size (from $d_p \sim 7$ μm to $d_p \sim 20$ μm); revealed that the fractal dimension of the agglomerates is close to $D = 2.5$ as predicted by the diffusion-limited particle-to-agglomerate aggregation model (DLA) introduced by Witten and Sander,[37] where self-similar fractal patterns ramify due to the irreversible sticking of particles in a random motion. Moreover, the derived size of agglomerates was shown to be in agreement with the theoretical prediction given by Eq. 7.[33]

The Harrison et al. equation (Eq. 2) can be modified for fluidized beds of agglomerates in order to estimate the ratio of the largest stable size of fluid bubbles D_b relative to the agglomerate size d^*. The modified equation that results from the balance of the rising velocity of a fluid bubble to the terminal settling velocity of an agglomerate v^* is

$$\frac{D_b}{d^*} \simeq \frac{1}{18^2\, 0.7^2}\frac{\rho_p^2\, g\, d_p^3}{\mu^2} Bo_g^{(2D-3)/(D+2)} \tag{10}$$

where we have used Eq. 7. Equation 10 will be employed in this work to describe the fluidization behavior of our

cohesive powders. According to Harrison et al. we should expect heterogeneous bubbling fluidization for $D_b/d^* \gtrsim 10$, whereas for $D_b/d^* \lesssim 10$, it is likely that the small gas bubbles developed do not coalesce into large bubbles for a range of gas velocities in which the bed exhibits uniform fluidization behavior. As the gas velocity is increased, and, consequently, the concentration of these small gas bubbles is increased, it should be expected that the coalescence mechanism leads to the onset of macroscopic bubbling.

The attractive force F_0 between uncharged particles fluidized by dry gas arises mainly from the van der Waals interaction.[25]

$$F_0 \simeq \frac{A d_a}{24 z_0^2} \tag{11}$$

where $z_0 \simeq 3 - 4$ Å is the distance of closest approach between two molecules, A is the Hamaker constant, and d_a is the typical size of the surface asperities. Typically $A \sim 10^{-19}$ J and $d_a \sim 0.2$ μm,[25] which gives an order of magnitude for $F_0 \sim 10$ nN. Surface coating with nanoparticles such as silica, may decrease the typical surface asperity size to the size of nanoparticle agglomerates in the surface, and thus, reduce F_0 down to $F_0 \sim 1$ nN.[38] If we use as typical values for fine powders $F_0 = 5$ nN, $d_p = 10$ μm, and $\rho_p = 1{,}000$ kg/m^3, Eq. 10 gives $D_b/d^* \simeq 4$ for fluidization with Nitrogen at 300 K ($\mu = 1.79 \times 10^{-5}$ Pa s) predicting a transitional behavior in agreement with our observation.[31] Therefore, it is clear that a change of gas viscosity may result in a qualitative change of fluidization behavior. For example, we would obtain $D_b/d^* \simeq 1.3$ for fluidization with Neon at 300 K ($\mu = 3.21 \times 10^{-5}$ Pa s), which, theoretically, should result in a qualitative improvement of fluidization uniformity and a delay (and possibly suppression) of the onset of bubbling. According to our estimations, when fluidizing at higher gas viscosities (or temperatures), and/or with smaller particle sizes ($D_b/d^* \lesssim 1$), the bubbling regime is expected to be fully suppressed.

Experimental data on the bubbling onset[31] also indicate that the initiation of visible bubbling can be predicted by a modified Wallis criterion for a fluidized bed of agglomerates. Using Eq. 7 we can write the modified Wallis criterion as[31]

$$\begin{aligned} u_\phi^* &\simeq \phi \frac{1}{18} \frac{\rho_p g d_p^2}{\mu} n \left(1 - \phi Bo_g^{(3-D)/(D+2)}\right)^{n-1} Bo_g^{2/(D+2)} \\ u_e^* &\simeq \left(g d_p \phi Bo_g^{(4-D)/(D+2)}\right)^{1/2} \\ u_\phi^* &< u_e^* \text{ nonbubbling regime} \\ u_\phi^* &\simeq u_e^* \text{ at bubbling onset} \end{aligned} \tag{12}$$

In this equation the effects of μ and Bo_g on the onset of bubbling are also apparent. If only particle size is varied, we would have $u_\phi^* \propto Bo_g^{0.22}$ $(1 - \phi Bo_g^{0.11})^{4.6}$ using $N = 5.6$, and $u_e^* \propto \phi^{0.5}$ independent of Bo_g (using $D = 2.5$). Accordingly u_ϕ^* decreases as Bo_g is increased, while u_e^* remains constant, thus, the value of ϕ, at which the bubbling onset condition is met decreases, or equivalently the bubbling gas velocity increases. The same reasoning applies to a change of gas viscosity since $u_\phi^* \propto \mu^{-1}$ and u_e^* does not depend on μ. Therefore, we are able to predict from both the Harrison and Wallis modified criteria, that a combination of large values of Bo_g and μ may eventually give rise to a full suppression of the bubbling regime, ie., the fluidized bed would transit directly from a nonbubbling fluidlike regime to elutriation.

Fluidization of nanoparticles

Recently it has been observed that in a fluidized bed of nanoparticles, complex-agglomerates form by a multistage process consisting of agglomeration of pre-existing simple-agglomerates.[39] The agglomeration process of the simple-agglomerates into complex-agglomerates may be described similarly to the agglomeration of fine particles by considering these simple-agglomerates as effective particles undergoing a process of agglomeration controlled by the balance between the local shear force and attractive force between simple-agglomerates. We then can obtain a modified version of Eq. 7

$$Bo_g^* \sim (k^*)^{D^*+2} \tag{13}$$

where $Bo_g^* = F_0^*/(k^D W_p)$ is the ratio of the attractive force between simple-agglomerates F_0^* to the weight of a simple-agglomerate, k is the ratio of simple-agglomerate size to primary particle size d_p, D is the fractal dimension of a simple-agglomerate ($k^D = N$ is the number of primary particles in a simple-agglomerate), k^* is the ratio of complex-agglomerate size d^{**} to simple-agglomerate size d^*, $D^* = \ln N^*/\ln k^*$ is the fractal dimension of the complex-agglomerate, and N^* the number of simple-agglomerates in the complex-agglomerate.

Likewise the Richardson-Zaki equation needs further modification as discussed elsewhere.[40] If we consider the light complex-agglomerates as effective particles and using the complex-agglomerate volume fraction ϕ^{**} we have[40]

$$v_g = v^{**}(1 - \phi^{**})^n \tag{14}$$

where $n \approx 5.6$ in the small Reynolds number limit as for the original R-Z correlation (Eq. 3). Taking into account the multistage structure of the complex-agglomerates, Eq. 14 can be rewritten as[40]

$$\frac{v_g}{v_{p0}} = \frac{N}{k} \frac{N^*}{k^*} \left[1 - \frac{k^3}{N} \frac{(k^*)^3}{N^*} \phi\right]^n \tag{15}$$

If we assume the existence of a global fractal dimension for the complex-agglomerate $D_a = \ln N^{**}/\ln k^{**}$, where $N^{**} = N N^*$ is the number of primary particles in the complex-agglomerate and $k^{**} = k k^*$ is the ratio of complex-agglomerate size to primary particle size, and allow that $D_a = D = D^*$, Eq. 15 can be further simplified to

$$\frac{v_g}{v_{p0}} = (k^{**})^{D_a - 1} (1 - (k^{**})^{3 - D_a} \phi)^n \tag{16}$$

This equation has been already used in other works to estimate the size of agglomerates in gas-fluidized beds of nanoparticles.[34,41]

In this work we will extend the Harrison et al. equation (Eq. 2), and Wallis equation (Eq. 4) to the case of agglomerate particulate fluidization of nanoparticles. As we did previously with the R-Z equation,[40] if we consider complex-agglomerates as effective particles, the Harrison et al. equation can be written as

$$\frac{D_b}{d^{**}} \simeq \frac{1}{18^2\,0.7^2}\frac{\rho_p^2\, g\, d_p^3}{\mu^2} k^{2D-3}\left(k^*\right)^{2D^*-3} \tag{17}$$

Assuming $D = D^* = D_a$, we may use the simplified equation

$$\frac{D_b}{d^{**}} \simeq \frac{1}{18^2\,0.7^2}\frac{\rho_p^2\, g\, d_p^3}{\mu^2} \left(k^{**}\right)^{2D_a-3} \tag{18}$$

Alternatively, we can take into account Eq. 13 and derive

$$\frac{D_b}{d^{**}} \simeq \frac{1}{18^2\,0.7^2}\frac{\rho_p^2\, g\, d_p^3}{\mu^2} k^{2D-3}\left(Bo_g^*\right)^{(2D^*-3)/(D^*+2)} \tag{19}$$

for the modified Harrison et al. equation. Likewise it is possible to write the modified Wallis criterion in terms of the granular Bond number Bo_g^*

$$\begin{aligned} u_\phi^{**} &\simeq \phi\frac{1}{18}\frac{\rho_p\, g\, d_p^2}{\mu} n k^2 \\ &\times \left[1-\phi k^{3-D}\left(Bo_g^*\right)^{(3-D^*)/(D^*+2)}\right]^{n-1}\left(Bo_g^*\right)^{2/D^*+2} \\ u_e^{**} &\simeq \left[g d_p \phi k^{4-D}\left(Bo_g^*\right)^{(4-D^*)/(D^*+2)}\right]^{1/2} \\ u_\phi^{**} &< u_e^{**} \text{ nonbubbling regime} \\ u_\phi^{**} &\simeq u_e^{**} \text{ at bubbling onset} \end{aligned} \tag{20}$$

or, if complex agglomerate size and fractal structure D_a are known, use the simplified version

$$\begin{aligned} u_\phi^{**} &\simeq \phi\frac{1}{18}\frac{\rho_p\, g\left(k^{**}\right)^2 d_p^2}{\mu} n\left[1-\phi\left(k^{**}\right)^{3-D_a}\right]^{n-1} \\ u_e^{**} &\simeq \left[g\left(k^{**}\right)^{4-D_a} d_p \phi\right]^{1/2} \\ u_\phi^{**} &< u_e^{**} \text{ nonbubbling regime} \\ u_\phi^{**} &\simeq u_e^{**} \text{ at bubbling onset} \end{aligned} \tag{21}$$

Therefore, it is clear that the widely accepted Geldart classification scheme for the behavior of fluidized beds solely based on particle-fluid density difference and particle size[24] cannot account for the influence of material and gas properties on fluidization, such as agglomeration due to interparticle forces and gas viscosity. These parameters are explicitly considered in Eqs. 10, 12, 19 and 20, which provide a phenomenological frame to predict whether fluidized beds manifest uniform fluidization, bubbling or elutriation.

Experimental measurements on fluidized beds of fine and ultrafine powders using nitrogen and neon as fluidizing gases will be presented later. In the Behavior of a fluidized bed of fine particles section, we show data on a fluidized bed of micrometric sized particles, and in the Behavior of fluidized beds of ultrafine particles section, experiments on nanoparticle fluidization are reported.

Experimental set-up

Materials

Experiments have been carried out using both micrometer sized powders and nanoparticles. We have used a commercially available xerographic toner (Canon CLC700 cyan toner) consisting of polyester particles ($d_p \simeq 8.3\ \mu$m, $\rho_p \simeq 1200$ Kg/m^3) as the micronsized powder. Part of the results from these experiments are reported in Ref. 42. We include them here to illustrate the analogous behavior between gas-fluidized beds of micronsized particles and gas-fluidized beds of nanoparticles. Two types of nanoparticles, which show contrasting fluidizing behavior, were tested; Aerosil R974 and Aeroxide TiO_2 P25. Aerosil R974 is a hydrophobic SiO_2 nanopowder with a particle density of $\rho_p = 2250$ kg/m^3, and a primary particle size of $d_p = 12$ nm. Aeroxide TiO_2 P25 is hydrophilic, has a particle density of $\rho_p = 4500$ kg/m^3, and a primary particle size of $d_p = 21$ nm. Previous reports[34,41] show that silica nanopowder exhibits agglomerate particulate fluidization (APF) behavior whereas titania nanopowder bubbles soon after the minimum fluidization velocity is surpassed (ABF behavior). APF is characterized by a large bed expansion and smooth fluidization, whereas ABF shows little bed expansion and large bubbles.[34]

Fluidization cells

Experiments were performed using two different fluidized bed setups: one at the New Jersey Institute of Technology (NJIT), described in detail in Ref. 34 and another at the University of Seville (Seville Powder Tester, SPT). We have used Nitrogen ($\mu = 1.79 \times 10^{-5}$ Pa s), and Neon ($\mu = 3.21 \times 10^{-5}$ Pa s) as the fluidizing gases at ambient conditions.

An extended report about the operation of the SPT fluidized bed apparatus can be found in Ref. 38. The fluidized bed of the SPT setup consists of a vertical 4.42 cm dia. vessel, 16.8 cm in height that is fitted at the bottom with a sintered metallic plate having a pore size of 5 μm, that acts as gas distributor. The powder in the vessel is subjected to a controlled flow of gas injected through the gas distributor at its bottom. The particle volume fraction ϕ is derived from the height of the bed, which is measured by an ultrasonic sensor placed on top of the vessel. This device can determine distance with an accuracy of ± 0.01 cm (much smaller than local fluctuations in bed height) by sending an ultrasonic wave and measuring the time of reflection from the target.

The NJIT fluidized bed setup consists of a vertical 5.08 cm dia. vessel, 152 cm in height that is fitted at the bottom with a sintered stainless steel plate having a pore size of 20 μm. The flow of gas to the column, either nitrogen or neon, was controlled with a mass flow meter. The pressure drop was measured by two taps in the column (one placed just above the distributor) using a transducer, and the bed height was measured with a scale as the gas velocity was slowly increased. A shorter version of this fluidization cell (23 cm in height) was used in the experiments of laser imaging of agglomerates that will be described later.

While Canon CLC700 was tested only at the SPT, silica R974 and titania P25 were tested in both setups. Before the experiments were performed, the particles were sieved (using a sieve opening of about 500 μm) in order to remove previously existing very large agglomerates. The length of the NJIT vessel allowed for the use of a larger amount of powder and thus a deep fluidized bed. While in the SPT shallow bed the masses of powder used were about 1 gram for silica and 4 grams for titania, the typical masses used in the NJIT fluidized bed were around 10 grams for both powders. In the case of silica, this reduces the relative error due to the considerable elutriation of particles at high-gas velocities. Furthermore channels are less stable in deep beds, which might

contribute for further expansion in the case of titania, a powder that exhibits heterogeneous fluidization. On the other hand, the SPT allowed for the use of the ultrasonic sensor to measure the settling velocity of the fluidized bed as done for the toner powders. Additionally, fluidization in both setups was carried out by different procedures. In the SPT setup the bed is previously subjected to a high-gas velocity, and then the gas velocity is abruptly decreased to the desired value. In the NJIT setup the gas flow is smoothly increased from zero allowing the bed to reach a stationary state and once the highest desirable gas velocity is achieved, the gas flow is smoothly decreased back to zero. It is well known that powder history may have substantial effects on the fluidization behavior of fine powders.[11] In the case of highly cohesive powders, interparticle adhesive forces are largely increased by stresses applied during powder history and, as a consequence, large coherent fragments of the consolidated powder are difficult to break by the gas. This suggests the classical Geldart C behavior characterized by strongly heterogeneous fluidization (rising plugs, rat holes, channeling, etc.). Thus, for these powders the fluidization procedure should have an effect on the powder behavior. On the contrary, for low-cohesive powders, the fluidization procedure should not influence the behavior of the powder.

Local solid fraction measurement

In addition to the overall fluidization behavior, the effect of gas viscosity was studied by measuring the local concentration of solids in a fluidized bed by monitoring the backscattered light intensity (reflectance R) collected by an optical probe as detailed described in Ref. 43. These experiments were done only in the SPT setup. The optics system consisted of a fiber optic reflection probe coupled to a spectrometer and a tungsten-halogen light source. The probe is a tight bundle of 7 optical fibers (an hexagonal array of 6 illumination fibers disposed around 1 read fiber 400 μm in dia.) embedded in a stainless steel 6.4 mm dia. ferrule with a 30° window to remove specular reflection effects. Although unavoidable flow perturbation is introduced by the probe downstream we expect it to be negligible upstream for its sharp "V" shaped tip, and as suggested by the similarity between our results and results from noninvasive local pressure measurements on a fluidized bed of glass beads.[45] We inserted the probe vertically at a depth of 1 cm in the center of the fluidized bed and the backscattered light intensity (named hereafter as reflectance R) at a wavelength of 550 nm was acquired each 24ms. According to our previous experiments, fluctuations in R can be directly related to fluctuations in the local density.[43] The characteristic frequency of fluctuations in the pressure due to gas bubbles in most bubbling beds is on the order of 1–5 Hz,[44] and, therefore, sampling with 1/24 ms $\simeq$ 40 Hz would be sufficient to detect not only large bubbles, but also small gas bubbles if they were present in the nonbubbling fluidlike regime.

Laser imaging of agglomerates

The direct measurement of the agglomerate size was performed at NJIT. The images of the agglomerates were recorded using a FlowMaster 3S CCD camera controlled by DaVis image acquisition and processing software. The Flowmaster camera was fitted with a variable magnification optics, allowing for a field of view ranging between 0.455 mm and 7.1 mm. The field of view used in the experiment was typically 3 mm. For illumination, we have used a Melles Griot He-Ne continuous laser (power 10 mW), whose beam was expanded into a laser sheet using a cylindrical lens (f = −50). The laser sheet was oriented in the vertical direction and the Flowmaster camera was aligned perpendicular to it, pointing slightly downwards towards the surface of the fluidized bed. The cylindrical lens was placed far enough from the camera, so that the field of view of the camera fitted into the width of the laser sheet.

During the experiment, it is important to keep the surface of the fluidized bed close to the spot where the camera is focusing since the images could only be taken in the splash zone just above the surface of the fluidized bed. Images of the agglomerates were acquired at 8 frames per second. The exposure time of each image is 1 ms for the experiments with silica R974 and 0.5 ms for titania P25. In the case of silica R974, the superficial gas velocity was 1.37 cm/s, equivalent to a displacement of 13.7 μm during the exposure time. For titania P25, the superficial gas velocity was 1.37 cm/s in the case of fluidization with nitrogen and 1.26 cm/s with neon, equivalent to a displacement of 6.85 μm and 6.30 μm, respectively.

The images from the Flowmaster camera have a dynamic range of 4096 arbitrary intensity units. At the conditions where the experiments were performed, the noise level in the images is at the level of approximately 55 intensity units with standard deviations of the order of 2 intensity units. Those images whose maximum intensity were 64 intensity units were discarded as not being useful for agglomerate size determination. On the other hand, no images with intensities larger than 512 units were found in the experiments. Once the low-quality images were discarded, the remaining images were rescaled into 256-gray levels images (scaling the maximum intensity of the image to the 256th gray level), and thresholded using a C/C++ routine to convert them into pure black and white images.

The final step was to measure the agglomerate sizes in the thresholded images. This was done using the public domain program ImageJ[46] using the "segmented area of interest" tool to outline the agglomerate. ImageJ automatically determines the area A inside the outline. The agglomerate size d_i is taken as the diameter of the circle with the same area A_i as the agglomerate.

From the distribution of agglomerate sizes d_i, two types of characteristic diameters of the agglomerates can be found: the number-length average diameter d^{NL}, and the surface-volume average dia. d^{SV}. The number-length average diameter is defined simply as the average of the individual sizes d_i, while the surface-volume average diameter is found from

$$d^{SV} = \frac{\sum_i d_i^3}{\sum_i d_i^2} \tag{22}$$

which turns to be the diameter of a sphere having the same ratio of surface to volume as the particles. Since the weight of an agglomerate depends on its volume, and the drag that it experiences depends on its surface, the most relevant average diameter used to compare with the results obtained from

the modified R-Z equations is the surface-volume average diameter.

Experimental Results

Behavior of a fluidized bed of fine particles

As previously stated, Canon CLC700 toner was used as a model micrometric powder. All experiments with Canon CLC700 were performed in the SPT setup.

Fluidization Regimes. Figure 1 displays data of the particle volume fraction ϕ vs. the superficial-gas velocity v_g. All the data are taken once the bed has arrived in a stationary state at v_g, which is imposed after the bed was conveniently initialized in a bubbling state in which it has lost memory of its previous history.[45] In Figure 1 we show the flow regimes that have been identified. The bed transits to a solidlike regime at $v_g \simeq 1$ mm/s for nitrogen fluidization and at $v_g \simeq 1.8$ mm/s for neon fluidization. While in the interval $v_g \in (1, 1.8)$ mm/s the bed fluidized with neon is in a stable solidlike regime, the regime is heterogeneous when it is fluidized with nitrogen. This heterogeneous state is characterized by long-lived solid network structures coexisting with transient craters and volcanoes. A footprint of such structures is seen in the local reflectance time signals $R(t)$, where time periods of low-reflectance, due to the opening of craters, alternate with time periods of higher reflectance and small fluctuations typical of the solidlike behavior. In the window $v_g \in (1.8, 2.5)$ mm/s fluidization is heterogeneous for both gases and the experimental data of ϕ vs. v_g are, within the experimental scatter, in the same curve. Between 2 mm/s and 3 mm/s, nitrogen fluidization turns gradually from heterogeneous to uniform fluid-like type. The standard deviation of $R(t)$ decreases markedly, but in this window, we still see relatively important fluctuations in the bed height. These fluctuations in bed height decline gradually as v_g is increased. In the interval between 2.5 mm/s and 3 mm/s a novel phenomenon is observed when the powder is fluidized with neon.

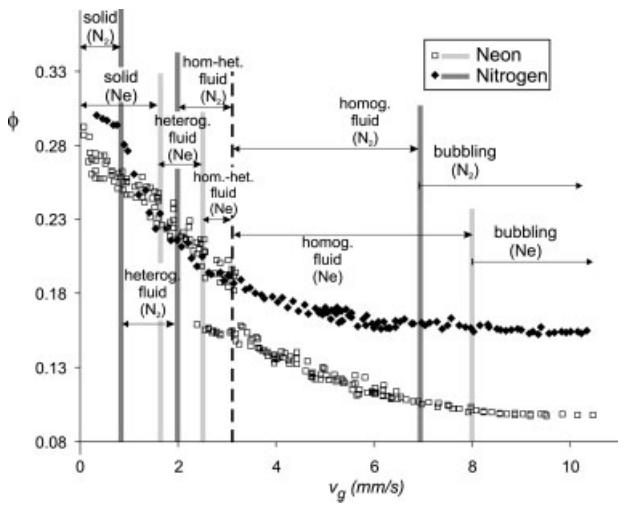

Figure 1. Particle volume fraction ϕ vs. gas velocity v_g for neon and nitrogen fluidization of toner Canon CLC700.

Fluidization regimes are delineated.

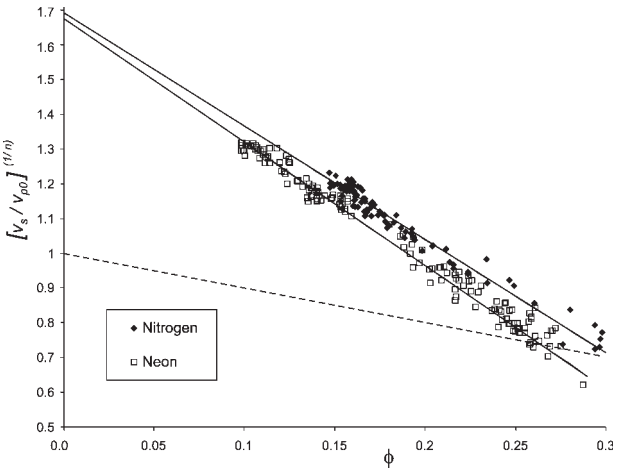

Figure 2. Settling velocity v_s of the fluidized bed (relative to the settling velocity of an individual particle and raised to the power of 1/5.6) vs. particle volume fraction for nitrogen and neon fluidization of toner Canon CLC700.

The solid lines are the best fits curves of the modified R–Z law to the data. The dashed line is the R–Z prediction for individual particles.

The fluidized bed in this interval cannot reach a stationary state, flipping back and forth between heterogeneous ($\phi \simeq 0.18$) and uniform fluidization ($\phi \simeq 0.15$). For 3 mm/s $< v_g < v_{mb}$, where v_{mb} is the gas velocity at the onset of bubbling, fluidization is uniform and the bed height decreases smoothly as v_g is decreased.

Settling Experiments. Agglomerate Properties. According to theory (Eq. 7), gas viscosity should not affect the agglomerate size (although the interparticle force F_0 might increase by gas adsorption to the surface of the particles, this effect is negligible at ambient pressure).[47] In order to check that, settling experiments, which consist of suddenly stopping the gas flow after the fluidized bed has reached a stationary condition, have been performed. In Figure 2 we show data of the initial settling velocity of the bed v_s vs. the particle volume fraction ϕ. Figure 3 is a plot of v_s vs. v_g, where it is seen, as expected, that $v_s \simeq v_g$ in the uniform fluidization regime, whereas $v_s < v_g$ in bubbling fluidization. The R-Z law for individual non-agglomerated particles is also plotted (in Figure 2) showing that it clearly underestimates the experimental settling velocity in the fluidlike regime. On the other hand, the data can be well fitted by a modified Richardson-Zaki (R-Z) law (Eq. 9) for agglomerated particles. The solid lines plotted in Figure 2 correspond to the best fits of the modified R-Z law to the data. These best fits yield similar values of N and k for fluidization with both gases: $N = 114.7$, $k = 6.05$ (for nitrogen fluidization) and $N = 109.8$, $k = 6.15$ (for neon fluidization). We also have not observed clear differences between agglomerates taken out from the bed and visualized at the optical microscope (following the procedure described in Ref. 38). Thus, it can be concluded that there is not a relevant distinction between the agglomerates fluidized with different gases as theoretically predicted. The settling velocities of the bed in the bubbling regime also

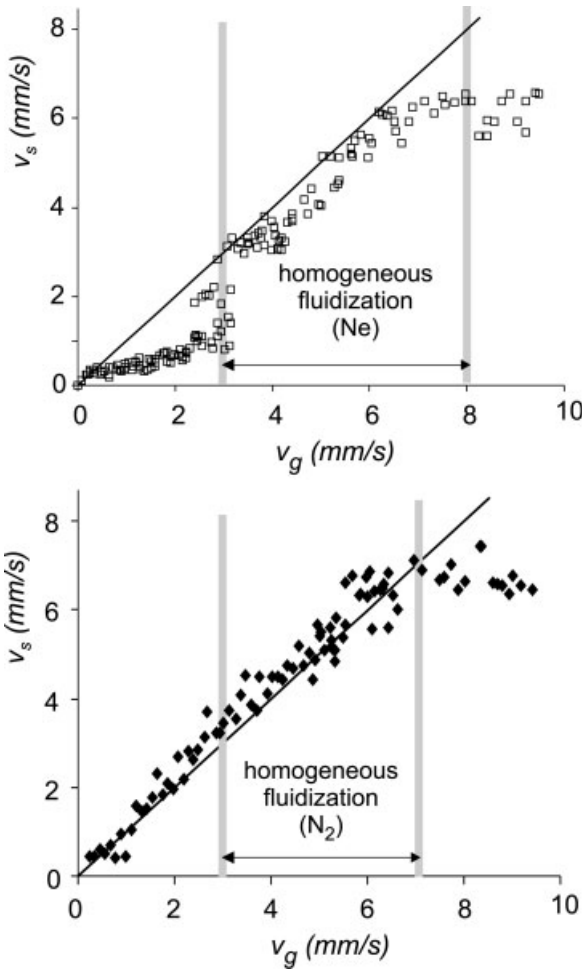

Figure 3. Settling velocity of the fluidized bed v_s vs. gas velocity v_g for neon fluidization (top), and nitrogen fluidization (bottom) of toner Canon CLC700.

fit to the modified R-Z equation, suggesting that the agglomerates are not significatively affected by bubbling.

Using the values of N and k derived from Eq. 7 we estimate $F_0 \sim 10$ nN, which is of the same order of magnitude as the value for F_0 estimated earlier from the van der Waals force given by Eq. 11. (Interparticle capillary forces are negligible since we use dry gas.) From charge spectrograph measurements it can also be concluded that electrostatic forces are negligible as reported in the literature for electroneutral fine powders.[25,48]

Analysis of the Local State. Figure 4 displays typical time signals of the local reflectance $R(t)$ detected by the local probe for different fluidization regimes using neon as fluidizing gas. The main features in the nonbubbling regime are the sudden drops in R due to the passage near the optical probe of small gas bubbles, which are not able to reach a macroscopic size (see Ref. 43 for a detailed discussion). The time signals obtained in this regime are qualitatively similar for fluidization with both gases, however, we observe that the drops in the reflectance are larger for fluidization with nitrogen in the vicinity of the transition to uniform fluidization.

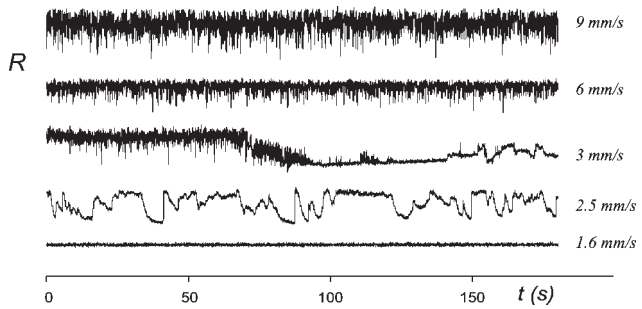

Figure 4. Typical time series of the local reflectance (in a.u.) measured by an optical probe for different fluidization regimes of toner Canon CLC700 in neon fluidization.

From top to bottom: bubbling, uniform fluidization, uniform to heterogeneous fluidization transition, heterogeneous fluidization and solid (gas velocities are attached to each curve).

This is clearly seen in Figure 5, in which time signals of the reflectance are plotted for fluidization with both gases at the same gas velocity. In Ref. 43 we developed a simple algorithm in order to quantify the frequency of these small gas bubbles detected by the local probe (see Ref. 43 for details). Results of the average number of small gas bubbles per unit time (f) are plotted in Figure 6 along with the standard deviation (σ) of the time signals for fluidization with both gases. Note that f and σ, which are mainly determined by the size and frequency of the drops in the reflectance, are clearly correlated. It is seen in Figure 6 that near the heterogeneous fluidization regime $f_{Ne} < f_{N_2}$. The curves for both gases tend to converge as v_g is increased. As the onset of nitrogen-bubbling is approached we have $f_{Ne} \simeq f_{N_2}$ and $\sigma_{Ne} \simeq \sigma_{N_2}$ (see Figure 6). At the nitrogen-bubbling onset the coalescence of small gas bubbles dominates over the splitting process, and f_{N_2} saturates. On the contrary f_{Ne} keeps growing, and, consequently, the neon-bubbling onset is further delayed. However, we must note that the transition from small gas bubbles to large gas bubbles is not sharply defined. As seen in Figures 1, 3, and 6 the system approaches the bubbling regime gradually, in analogy with the behavior of liquid-fluidized beds of high-density beads.[9]

Discussion. The role of Gas Viscosity and Particle Agglomeration. The improvement of fluidization uniformity and delay of visible bubbling must be a consequence of the enhancement of the local gas-bubble splitting mechanism, reminding us of the efficiency of bubble breakup observed in liquid-fluidized beds.[9] In order to make some estimations of

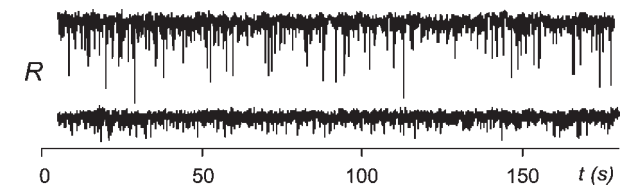

Figure 5. Local reflectance (in a.u.) in the nitrogen-fluidized bed (top), and neon-fluidized bed (bottom) of toner Canon CLC700 for v_g = 4 mm/s.

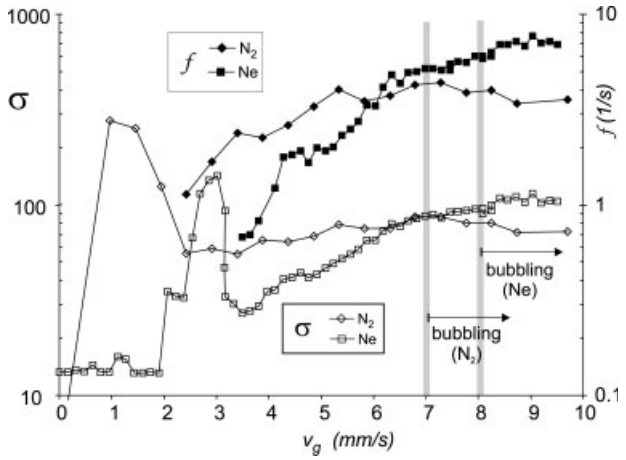

Figure 6. Standard deviation σ (left axis), and average number of reflectance drops per unit time f (right axis) vs. gas velocity v_g for nitrogen and neon fluidization of toner Canon CLC700.

the largest stable size of a single gas bubble we will use the empirical criterion of Harrison et al., modified for agglomerate particulate fluidization (Eq. 10). Calculations yield $D_b \simeq 480\ \mu\text{m} \sim 10\ d^*$ (nitrogen fluidization), and $D_b \simeq 130\ \mu\text{m} \sim 3d^*$ (neon fluidization). Both numbers lead us to expect a transitional behavior as seen experimentally.

The smaller maximum size of stable gas bubbles in neon explains why far from bubbling, where the concentration of small gas bubbles is not high, and their collective interaction is negligible, we observe a qualitative difference between the sizes of small gas bubbles in neon and nitrogen that is reflected, at the macroscopic level, in the difference of bed expansion. Due to the smaller size of the local gas bubbles in neon, their critical concentration (or frequency) for coalescing into large bubbles must be higher, thus, allowing the bed to achieve further expanded states. Since the resistance of the swarm of solids surrounding the gas bubble to be diluted should increase with gas viscosity, a possible explanation would be the increase of the coherence of the swarm of agglomerates that approaches the gas bubble and destabilizes it. Coherent solid jets can make indentations more easily at a small gas bubble instead of flowing around it. The physical picture would consist of rising small gas bubbles rapidly split by coherent solid jets before being able to coalesce into large bubbles. As a result we have at the maximum expanded state $\phi = \phi_b \simeq 0.155$ and $f \simeq 4\ s^{-1}$ for nitrogen, whereas $\phi = \phi_b \simeq 0.096$ and $f \simeq 8\ s^{-1}$ for neon.

In Figure 7 we show the predicted particle volume fraction for our powder at the initiation of bubbling from the modified Wallis criterion (Eq. 12) as a function of gas viscosity. It is seen that the bubbling condition ($u_e^* = u_\phi^*$) is met for theoretical values of ϕ close to the experimental ones for the two gases experimentally tested (nitrogen and neon). Figure 7 predicts the suppression of the bubbling regime for $\mu \gtrsim 3.8 \times 10^{-5}$ Pa s. In this limit it would be expected that the fluidized bed experiences a direct transition from uniform fluidization to elutriation, which is reminiscent of the behavior of moderate-density beads fluidized by liquid.[9] On the other hand, Figure 7 shows that $\phi_b \gtrsim 0.2$ for $\mu \lesssim 1 \times 10^{-5}$ Pa s (as in the case of H_2 for example), which is close to the particle volume fraction at the transition to the fluidlike regime (see Figure 1). In this low-viscosity limit bubbling would initiate shortly after the solid to fluid transition, in agreement with the prediction from the modified Harrison criterion ($D_b \sim 30\ d^*$ for $\mu = 1 \times 10^{-5}$ Pa s).

Behavior of fluidized beds of ultrafine particles

Aerosil R974 and Aeroxide TiO_2 P25 were used as typical ultrafine materials. In this section we present the results on the fluidization behaviour of both materials, and also on the direct agglomerate imaging. Fluidization experiments with both materials were carried in the SPT setup and the NJIT setup. Laser agglomerate measurement was performed entirely at the NJIT.

Fluidization of Silica Nanoparticles. Figure 8 displays data of the particle volume fraction ϕ as a function of superficial gas velocity v_g for fluidization of Aerosil R974, with nitrogen and neon at ambient conditions. When the gas velocity is suddenly decreased from a high-value down to a value smaller than $v_g = v_J \simeq 0.4$ cm/s (as done in the SPT); the fluidized bed gets jammed in a solidlike expanded state. In this solidlike fluidized state the bed retains a small but nonvanishing yield strength due to the enduring contacts established between the jammed agglomerates. On the other hand, when the gas velocity is slowly increased from zero (as done at NJIT), we see that the bed channels very badly at low-gas velocities (pressure drop is unstable), which prevents its expansion until it transits to the uniform fluidlike regime. Hysteresis in the fluidlike regime ($v_g \gtrsim 0.4$ cm/s) is then erased and both sets of data adjust to the same trend in the fluidlike regime, in which the bed is uniformly fluidized, macroscopic bubbles are not visible, and the gas pressure adjusts to the powder weight per unit area. In this regime, the height of the free surface and the mass of elutriated powder increase monotonically as the gas velocity is

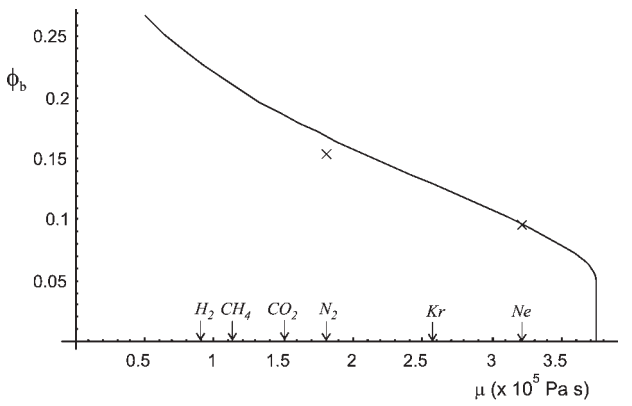

Figure 7. Predicted particle volume fraction at the onset of bubbling for fluidization of Canon CLC700 xerographic toner as a function of gas viscosity.

Experimental values of the bubbling points for fluidization with nitrogen and neon are also plotted. Viscosities of some gases at ambient conditions ($T = 300$K) are indicated.

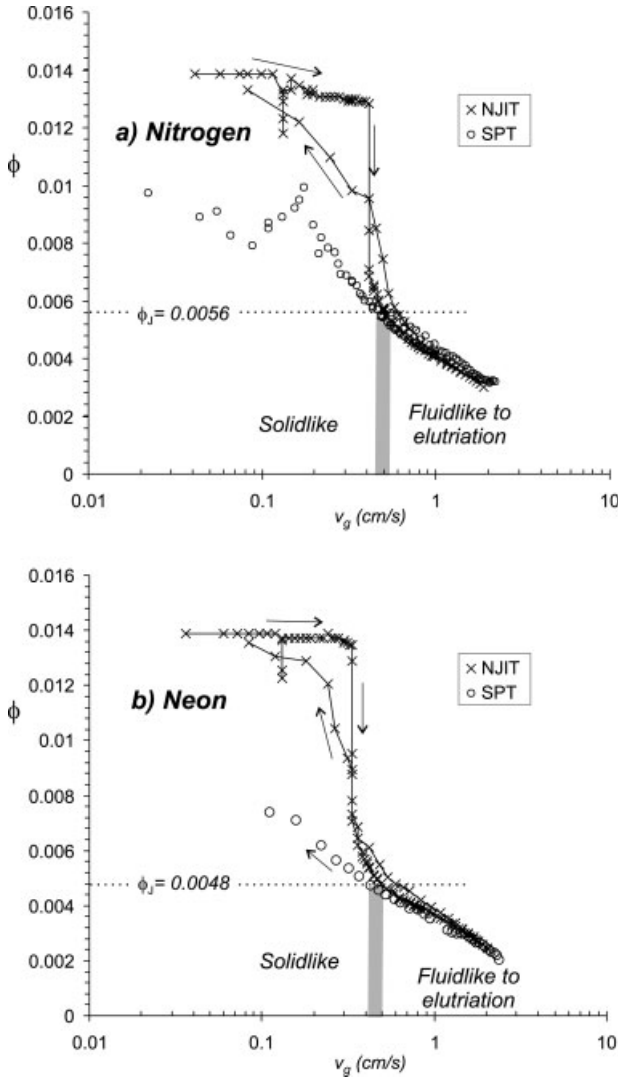

Figure 8. Particle volume fraction ϕ as a function of superficial gas velocity v_g for fluidization of Aerosil R974 with nitrogen (a), and neon (b) at ambient conditions from the SPT and NJIT setups.

In the NJIT experiments the gas flow is smoothly increased from zero and then decreased again to zero (as indicated by the arrows). In the SPT setup the gas flow is suddenly decreased after the bed has been fluidized at the higher gas velocity ($v_g \simeq 3$ cm/s). Fluidization regimes have been delineated. ϕ_j indicates the jamming transition.

increased, and, thus, we observe a full suppression of the bubbling regime, i.e., the fluidized bed transits gradually to elutriation. The passage to the fluidlike regime occurs at $\phi = \phi_J \simeq 0.0056$ for fluidization with nitrogen, and at $\phi = \phi_J \simeq 0.0048$ for fluidization with neon, indicating that the increase of gas viscosity produces higher bed expansion in the fluidlike regime as we had anticipated. This is clearly shown in Figure 8, in which we compare data from fluidization with both gases.

In Figure 9 we show data of the settling velocity v_s of the fluidized bed of Aerosil R974 measured just after suddenly stopping the gas flow as a function of the superficial gas velocity v_g at which the bed was fluidized. The data corresponds to measurements performed in the SPT setup, in which bed height h is detected at a frequency of 40Hz by the ultrasonic emitter-receiver placed on top of the bed as the bed is settling. This plot shows that fluidization in the fluidlike regime is quite uniform since the data fits pretty well to the straight line $v_s = v_g$. Thus we can use the gas velocity in the modified R–Z equation for fluidization of the silica nanoparticles (Eq. 16). Figure 10 is a plot of $(v_g/v_{p0})^{(1/n)}$ vs. ϕ showing that the modified R–Z equation (Eq. 16) can be considered as a good fit to the data. Moreover, it is seen that, within the experimental scatter, the data on fluidization with neon and data on fluidization with nitrogen are on the same trend, indicating that the properties of the agglomerates do not depend essentially on the type of gas as theoretically expected (Eq. 13). From these fits we obtain: $N^{**} \simeq 2.31 \times 10^{11}$, $k^{**} \simeq 25766$ (fluidization with nitrogen), and $N^{**} \simeq 3.68 \times 10^{11}$, $k^{**} \simeq 31145$ (fluidization with neon). Assuming that the complex-agglomerate can be characterized by a global fractal dimension $D_a = \ln N^{**}/\ln k^{**}$, these values would give $D_a \simeq 2.576$ (fluidization with nitrogen), and $D_a \simeq 2.574$ (fluidization with neon). These values agree with the reported result by Nam et al. ($D_a = 2.57$, see Ref. 41), derived also by fitting their experimental results on vibrofluidized bed expansion to the modified R–Z equation. Wang et al.[50] have recently used particle image velocimetry analysis and laser based planar imaging to measure the terminal settling velocity and size of single agglomerates of nanoparticles formed in the fluidized bed. By relating both measurements they have obtained that 84% of the agglomerates have fractal dimensions of 2.5 ± 0.07, while the lower and upper limits were found to be about 2.3 and 2.73.

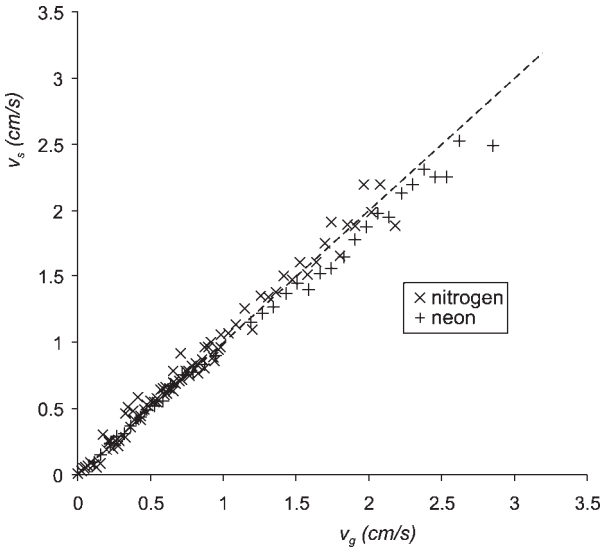

Figure 9. Initial settling velocity v_s as a function of superficial gas velocity v_g for fluidization of Aerosil R974 with nitrogen and neon at ambient conditions in the SPT setup (shallow bed).

v_s is measured just after the gas flow supply is suddenly stopped. The dashed line represents the function $v_s = v_g$.

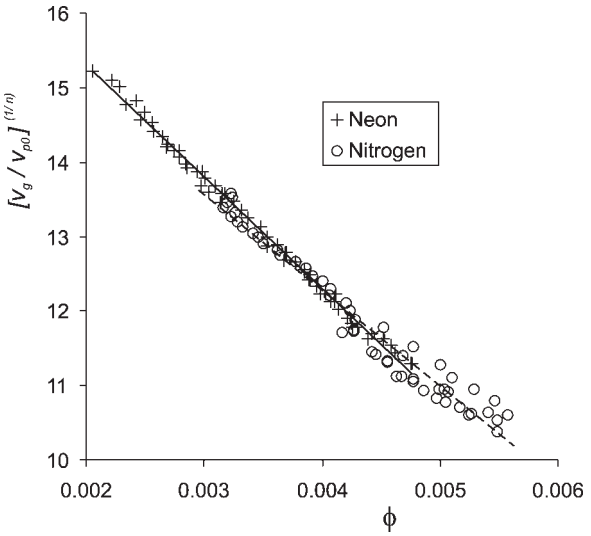

Figure 10. Ratio of gas velocity v_g to the settling velocity of an individual particle v_{p0} to the power of 1/5.6 as a function of the particle volume fraction ϕ for neon and nitrogen fluidization in the fluidlike regime of silica nanopowder.

The solid line represents the best linear fit to the data on neon fluidization. The dashed line represents the best linear fit to the data on nitrogen fluidization.

The values derived for the size of the complex-agglomerates from these bulk measurements are $d^{**} = k^{**}d_p \simeq 309$ μm (fluidization with nitrogen), and $d^{**} \simeq 373$ μm (fluidization with neon), which are similar to the value measured in-situ by Zhu et al.[34] with the aid of a laser source focused on the bed surface fluidized with nitrogen ($d^{**} \simeq 315$ μm).[34]

Direct Imaging of Silica R974 Agglomerates. Figure 11 shows an image of silica R974 agglomerates fluidized by nitrogen after the thresholding procedure has being applied. In Figure 12 we present the distribution of agglomerate sizes measured from thresholded images for fluidization using nitrogen and neon. Image thresholding and agglomerate size measurement techniques were detailed in the Laser imaging of agglomerates section. The agglomerate size d_i is taken as the diameter of the circle with the same area of the agglomerate measured in the images. In the case of nitrogen fluidization, 704 agglomerates were recorded, while for neon fluidization the number of agglomerates was 245.

For both nitrogen and neon fluidization, the distributions of agglomerate sizes are asymmetric, showing a tail for large agglomerate sizes, a peak for intermediate sizes and tending towards zero for small agglomerate sizes. The experimental distributions can be fitted using least squares to the functional form

$$f(d) = \frac{1}{b^a \Gamma(a)} d^{a-1} \exp\left(\frac{-d}{b}\right) \tag{23}$$

with $a = 7.7$, $b = 18.6$ μm for nitrogen fluidization, and $a = 15.4$, $b = 10.1$ μm for neon fluidization. Thus, although the agglomerate sizes distributions for the fluidization with the two gases have similar appearance, they do not have exactly the same shape. The difference most likely arises from a smaller proportion of fines in the case of neon fluidization.

The number-length average diameters (d^{NL} as defined in the Laser imaging of agglomerates section) determined from the distributions are quite similar for the fluidization with the two gases. The values obtained were $d^{NL} = 144.1$ μm, (standard deviation $\sigma = 77.6$ μm) for fluidization by nitrogen, and $d^{NL} = 147.0$ μm, (standard deviation $\sigma = 42.2$ μm) for fluidization by neon. Thus, as inferred from bed expansion experiments, the average agglomerate size measured by this method is not significantly affected by the gas viscosity. Moreover, the numerical values obtained agree with the experimental results recently reported by Wang et al. for the same system and using also laser based planar imaging ($d^{NL} \simeq 147.0$ μm, see Ref. 51). On the other hand, the shape of the distributions obtained by us differ from the shape of the distributions presented by Wang et al.[51] Wang et al. show distributions in which the frequency of a given agglomerate size decreases monotonically as the size increases, indicating a large proportion of small agglomerates detected.

As with respect to the surface-volume average diameter (d^{SV} as calculated from Eq. 22), it is worth noting that this value is quite sensitive to the shape of the tail of the distribution. The exclusion of just a few of the largest agglomerate diameters from the distribution tail can alter the surface-volume average diameter significantly. In order to avoid this important source of error we have chosen to calculate

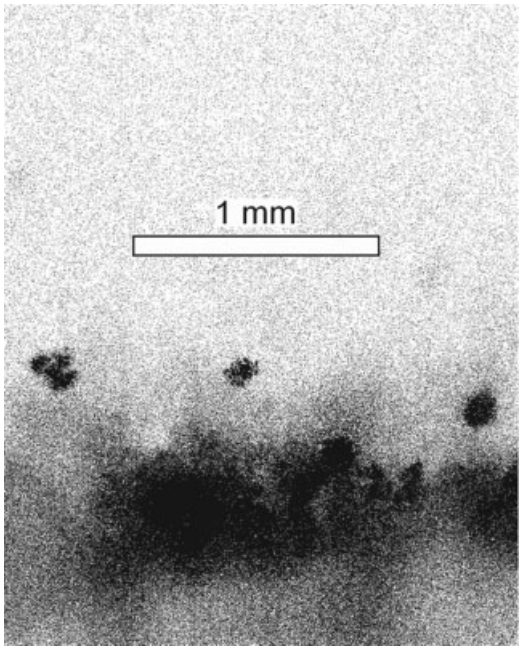

Figure 11. Image of agglomerates of silica R974 in the freeboard above the fluidized bed as obtained with the Flowmaster 3S camera, and the DaVis acquisition software and after application of the thresholding algorithm.

The exposure time to take the image is 1 ms. The example corresponds to fluidization by nitrogen at a superficial gas velocity $v_g = 1.37$ cm/s.

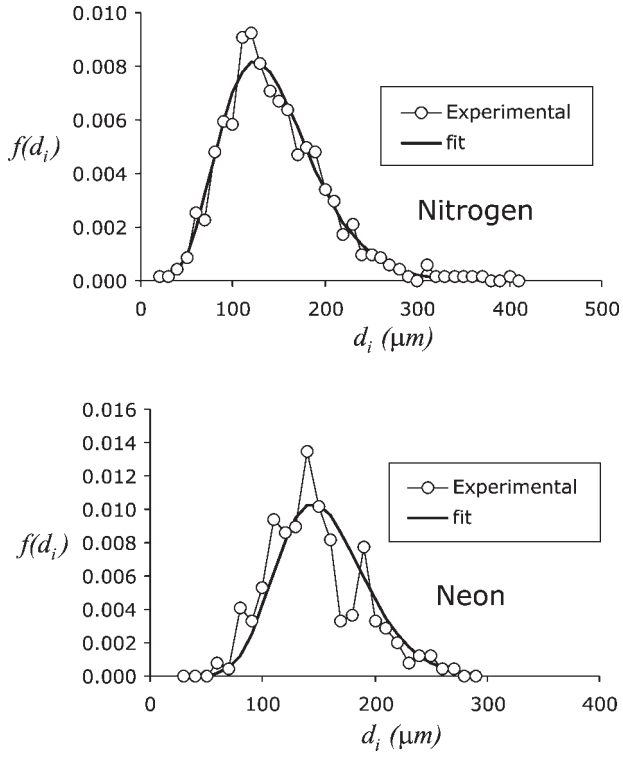

Figure 12. Agglomerate size distributions measured for silica R974 in fluidization by nitrogen (top) and neon (bottom).

(Agglomerate size measurement is based on the diameter of the circle d_i with the same area that the agglomerate as detailed in the Laser imaging of agglomerates section). The circles correspond to the experimental data. The solid line corresponds to a Poisson-like distribution fitted to the experimental data. Both distributions are normalized to unity. The parameters of the fit are given in the Behavior of fluidized beds of ultrafine particles section.

the surface-volume average diameter from the fitted distributions rather than directly from the experimental data. In this way we have found $d^{SV} = 180.4$ μm for fluidization by nitrogen, and $d^{SV} = 175.7$ μm for fluidization by neon. The similarity between these values again indicates that the viscosity of the fluidizing gas does not influence significatively the size of the agglomerates as theoretically predicted. On the other hand, the surface-volume average diameters reported by Wang et al.[51] are larger ($d^{SV} \simeq 240$ μm, see Ref. 51). The reason has to be found in the faster decay of the size distributions measured by us.

The smaller size of the superficial agglomerates measured from the laser-based planar imaging as compared to the average size of agglomerates derived from the R–Z fit to bed expansion data (309 μm and 373 μm for fluidization with nitrogen and neon, respectively) could be attributable to stratification of the agglomerates. In the stratified bed the largest size agglomerates would be at the bottom, and the successive layers toward the top would be composed of agglomerates of ever decreasing sizes, with the smallest ones preponderant at the very top. The sample of agglomerates recorded in the images would, therefore, be a sample biased towards smaller sizes.

Theoretical Estimation of Agglomerate Size in the Fluidized Bed of Silica. We can take as typical values for fluidization of silica nanoparticles: $d_p \simeq 12$ nm, $d^* \simeq 35$ μm (as inferred from the work by by Nam et al)[40,41], $\rho_p \simeq 2250$ kg/m^3, $F_0^* \simeq 10$ nN (as estimated from the van der Waals force, see Ref. 40). If we assume $D^* = D = D_a = 2.57$, as derived from bed expansion measurements in this work and also by Nam et al.[41], Eq. 19 predicts $d^{**} = 143$ μm. If we had used $D^* = D = D_a = 2.5$, the predicted value is $d^{**} = 165$ μm. These values are close to the average experimental values obtained from the laser imaging of the agglomerates. Let us note that the theoretical estimation does not consider the likely memory effects consisting of the persistence in the fluidized state of large agglomerates formed during powder history, and the agglomerates that remain most of the time close to the bottom of the bed. Thus, it is explainable that the theoretical estimation conforms to the laser imaging of agglomerates close to the bed surface.

Estimation of Maximum Bubble Size in the Fluidized Bed of Silica. Using the experimental values for agglomerate size from laser imaging (surface-volume average diameter), Eq. 18 yields $D_b/d^{**} \simeq 1.5$ and $D_b/d^{**} \simeq 0.4$, for fluidization with nitrogen and neon, respectively. In both cases, the absence of a bubbling transition which has been seen experimentally, would be predicted. Accordingly, from Eq. 20 it is obtained that $u_\phi^{**} < u_e^{**}$, $\forall \phi > 0$. Furthermore, in fluidization with neon D_b/d^{**} is smaller, which indicates an improvement of the quality of fluidization, as seen in the experiments. The same behavior would be predicted for fluidization with nitrogen at high-temperatures (for example at $T = 600$ K, $\mu = 2.96 \times 10^{-5}$ Pa s, similar to neon's viscosity at T = 300 K). Remarkably this change of behavior, as affected by gas temperature, might be of extraordinary relevance to gas-phase processes operated in a high-temperature environment that is routinely employed in the production of nanoparticles. On the other hand, the fluidization quality would be hampered, and the onset of a bubbling regime might be expected when fluidizing with low-viscosity gases.

Fluidization of Titania Nanoparticles. We have represented in Figure 13 data on the particle volume fraction ϕ vs. the superficial gas velocity for the nanopowder Aeroxide TiO_2 P25. In the deep bed (NJIT setup) it is observed that during fluidization, and after initial channeling, Aeroxide Titania P25 expands uniformly, but very quickly reaches a bubbling state during which large bubbles cause the bed height to remain constant or actually decrease when the gas velocity is further increased above the bubbling onset (see Figure 13). At the initiation of bubbling the bed had expanded to no more than twice the initial bed height and large bubbles rise up curtailing further expansion. This is in contrast with the smooth fluidization of silica nanopowder described in the previous section, characterized by a large bed expansion up to five times the original bed height, and a transition to elutriation instead of bubbling.

For titania, transition to bubbling is observed for fluidization with both gases. As expected, bed expansion is greater and bubbling is delayed to higher gas velocity for fluidization with neon as clearly observed when comparing Figure 13a and Figure 13b, for the NJIT data. Remarkably, hysteresis is found for this nanopowder also in the fluidlike regime indicating that fluidization uniformity is compromised even in the fluidlike state. This is especially relevant in the case of nitrogen, and as a result the hysteretic behavior in the fluid-

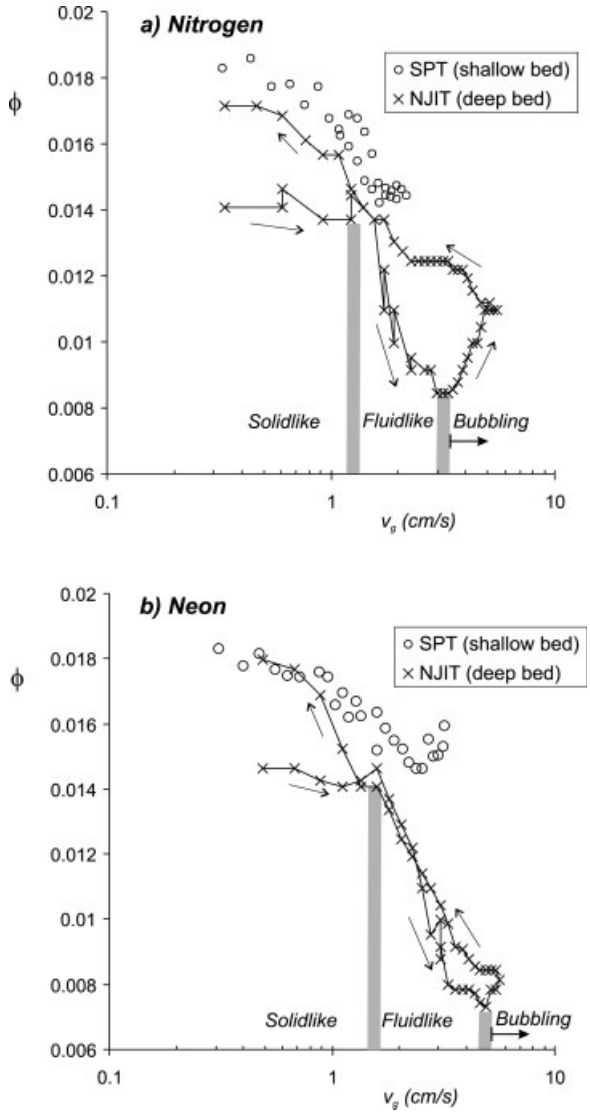

Figure 13. Particle volume fraction ϕ as a function of superficial gas velocity v_g for fluidization of Aeroxide Titania P25 with nitrogen (a), and neon (b) at ambient conditions from the SPT and NJIT setups.

In the NJIT experiments the gas flow is smoothly increased from zero and then decreased again to zero (as indicated by the arrows). In the SPT setup the gas flow is suddenly decreased after the bed has been fluidized at the higher gas velocity.

like regime is more pronounced for this smaller viscosity gas.

Another important difference with silica behavior is that results for fluidization of titania are poorly reproducible in the shallow bed used in the SPT setup. The height of the settled bed is about 3.7 cm, which is smaller than bed diameter (4.42 cm) in the SPT setup, whereas in the NJIT setup the height of the settled bed (about 7 cm) is larger than bed diameter (5.08 cm). Gas channels are more stable in the shallow bed, which hampers the quality of fluidization, thus, hindering bed expansion as seen in Figure 13. The heterogeneity of fluidization in the shallow bed may also be inferred from Figure 14 in which we plot the initial settling velocity of the fluidized bed v_s, measured by the ultrasonic sensor in the SPT setup, against the superficial gas velocity v_g. In contrast to the case of silica fluidization (Figure 9), we see a highly scattered cloud of data and mostly $v_s < v_g$, indicating that a relevant portion of the gas flow bypasses the bed through channels or bubbles corresponding to a poorly uniform fluidization.

Figure 15 is a plot of $(v_g/v_{p0})^{(1/n)}$ vs. ϕ for fluidization of titania nanopowder in the NJIT setup together with data of $(v_s/v_{p0})^{(1/n)}$ vs. ϕ measured in the SPT setup. Since, as demonstrated by Figure 13, fluidization was rather heterogeneous in the SPT setup ($v_s < v_g$), we have chosen to plot in this figure $(v_s/v_{p0})^{(1/n)}$, using the settling velocity measured in the SPT setup instead of gas velocity for the purpose of fitting the data to the R–Z equation. It is seen in Figure 15 that the data is highly scattered, which can be attributed to the fluidization heterogeneity. Also, we observe that, in contrast with the case of silica (Figure 10), the data for neon and nitrogen fluidization appear to be in different trends. This is an indication of the main effect of neon on improving the homogeneity of fluidization by destabilizing channels and decreasing the maximum size of bubbles, which prevents full expansion in the case of nitrogen fluidization. In fact, the scatter of the data on neon fluidization is appreciably reduced with respect to the scatter of the data on nitrogen fluidization.

In spite of the scatter of the data we may obtain just an estimation of the size of the agglomerates of titania nanoparticles fitting the modified R–Z law (Eq. 16) to the data in Figure 15. The values derived are: $N^{**} \simeq 1.43 \times 10^{10}$, $k^{**} \simeq 6945$, $d^{**} \simeq 146$ μm (fluidization with nitrogen), and $N^{**} \simeq 3.36 \times 10^{10}$, $k^{**} \simeq 9181$, $d^{**} \simeq 193$ μm, (fluidization with neon). The size estimated for these agglomerates is similar to the size

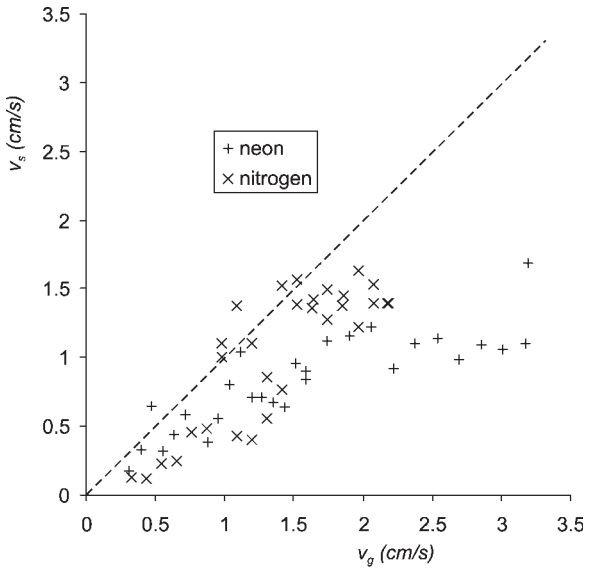

Figure 14. Initial settling velocity v_s as a function of superficial gas velocity v_g for fluidization of Aeroxide Titania P25 with nitrogen and neon at ambient conditions in the SPT setup (shallow bed).

v_s is measured just after the gasflow supply is suddenly stopped. The dashed line represents the function $v_s = v_g$.

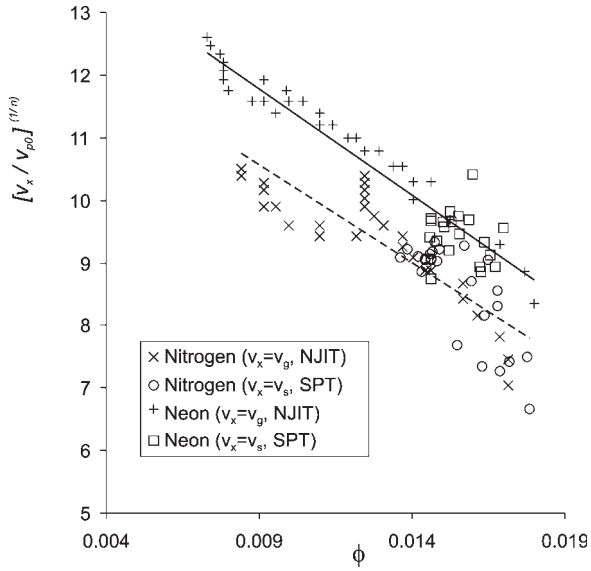

Figure 15. Ratio of gas velocity v_g to the settling velocity of an individual particle v_{p0} to the power of 1/5.6 as a function of the particle volume fraction ϕ for neon and nitrogen fluidization in the fluidlike regime of titania nanopowder measured in the NJIT setup.

For the SPT setup we plot the ratio of settling velocity v_s to v_{p0}. The solid line represents the best linear fit to the whole set of data on neon fluidization. The dashed line represents the best linear fit to the whole set of data on nitrogen fluidization.

reported by Zhu et al. from laser-based planar imaging measurements ($d^{**} \simeq 195$ μm).[34] Assuming that the complex-agglomerate can be characterized by a global fractal dimension $D_a = \ln N^{**}/\ln k^{**}$, the values estimated would give $D_a \simeq 2.65$ for fluidization with both gases. A remarkable observation is that the fractal dimension estimated for titania agglomerates is larger than the one estimated for silica agglomerates, indicating more compact agglomerates in the case of titania.

Direct Imaging of Titania Agglomerates. Figure 16 shows a thresholded image of Aeroxide TiO_2 P25 agglomerates in the freeboard of a bed fluidized with nitrogen. A general observation is that there is a larger concentration of agglomerates in the freeboard above the bed of titania than for the bed of silica. While for Aerosil R974 the surface of the fluidized bed was close to the position of the laser sheet, for Aeroxide P25 it was kept about 1 cm below the laser sheet. The reason is that the surface of the bed was irregular, with numerous volcanoes that would have interrupted the path of the laser if the surface were placed at the level of the laser sheet.

The number of images of agglomerates analyzed was 353 for nitrogen, and for 509 neon fluidization. The distributions of agglomerate sizes d_i found from the images is shown in Figure 17. Both for nitrogen and neon fluidization the data was fitted by Eq. 23, with $a = 3.7$, $b = 28.9$ μm for nitrogen, and $a = 3.2$, $b = 37.3$ μm for neon. The number-length average diameter d^{NL} obtained from these best fits were $d^{NL} = 110.2$ μm (standard deviation 63.9 μm) for nitrogen and $d^{NL} = 124.9$ μm (standard deviation 80.5 μm) for neon, suggesting again that the agglomerate size does not change significantly with a change in gas viscosity. The surface-volume average diameters obtained from the fits are $d^{SV} = 164.7$ μm for nitrogen and $d^{SV} = 194.0$ μm for neon. Generally, the agglomerate size distributions for titania (Figure 17) are wider than the agglomerate size distributions for silica (Figure 12).

Unlike for silica, the surface-volume average diameter found for titania agglomerates is roughly in agreement with the results from the settling experiments. But for titania, the volcanoes formed due to the poor fluidization ejected material from inside the bed on the surface of the bed through the region were the images were acquired. This circulation of material helps to bring agglomerates from the inside of the bed briefly into suspension, before the larger agglomerates fall back to the surface of the bed. Thus, for titania we expect the agglomerates recorded in the images to be a more representative sample of the agglomerates in the bulk of the stratified bed than for silica R974.

Theoretical Estimation of Agglomerate Size in the Fluidized Bed of Titania. The main difficulty in obtaining a theoretical value for the agglomerate size in the fluidized bed of titania is that we do not have a reliable estimation of the size of the simple pre-existing agglomerates of titania nanoparticles d^*. If we assume that, as for silica,[41] $d^* \approx 35$ μm, and the attractive force between simple-agglomerates is $F_0^* \approx 10$ nN, and assume $D^* = D = D_a = 2.65$, as derived from bed expansion measurements, Eq. 13 predicts $d^{**} = 101$ μm. If we had used $D^* = D = D_a = 2.5$, the predicted value is $d^{**} = 133$ μm. These values are of the same order of magnitude that the experimental values.

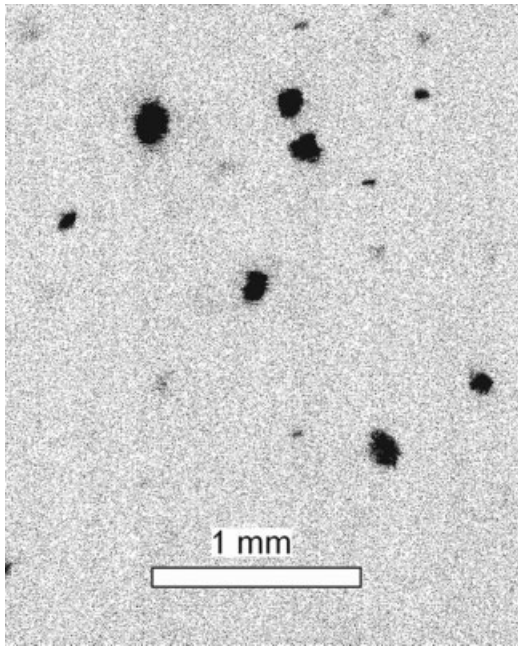

Figure 16. Image of the freeboard above the fludized bed of titania obtained with the Flowmaster 3S camera, and the DaVis acquisition software after application of the thresholding algorithm.

The exposure time of the image is 0.5 ms. The example corresponds to fluidization by nitrogen at a superficial gas velocity $v_g = 1.36$ cm/s.

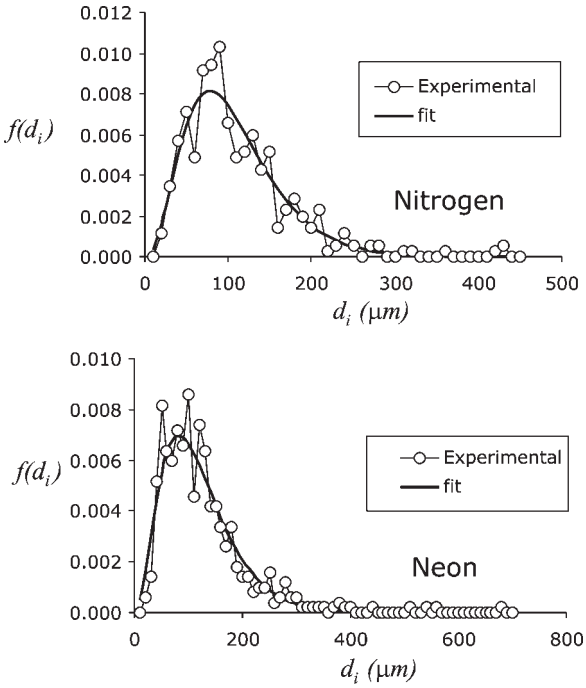

Figure 17. Agglomerate size distributions measured for titania P25 in fluidization by nitrogen (top) and neon (bottom). (Agglomerate size measurement is based on the diameter of the circle d_i with the same area that the agglomerate as detailed in the Laser imaging of agglomerates section).

The circles correspond to the experimental data. The solid line corresponds to a Poisson-like distribution fitted to the experimental data. Both distributions are normalized to unity. The parameters of the fit are given in the Behavior of fluidized beds of ultrafine particles section.

Estimation of Maximum Bubble Size in the Fluidized Bed of Titania. Using the experimental values of the agglomerate size from laser imaging (surface-volume average diameter), Eq. 18 yields $D_b/d^{**} \simeq 32.8$ and $D_b/d^{**} \simeq 14.8$, for fluidization with nitrogen and neon, respectively. According to the Harrison et al. criterion we should have expected bubbling fluidization for this nanopowder, especially marked for fluidization with nitrogen. Using the Wallis criterion, Eq. 20 predicts the initiation of bubbling at $\phi_b \simeq 0.018$ for fluidization with nitrogen. Note that this is approximately the value of the particle volume fraction of the settled bed in the shallow bed (SPT setup). This would have led us to expect that the bubbling onset occurs in parallel to bed expansion as seen experimentally. On the other hand, for fluidization with neon, it is calculated that $\phi_b \simeq 0.016$, which predicts bed expansion before the onset of bubbling as it is seen in the experiments. As described earlier, the deep bed used in the NJIT setup allows for further expansion than expected.

Concluding Remarks

The fluidization behavior of fine and ultrafine particles has been experimentally investigated. The powders tested consisted of micron sized polymer particles (particle size $d_p \simeq$ 8.3 μm), silica nanoparticles ($d_p \simeq 12$ nm), and titania nanoparticles ($d_p \simeq 21$ nm).

The fluidizing gases used have been nitrogen and neon, allowing us to study the effect of a change on gas viscosity by a factor of two approximately on fluidization behavior. Several experimental techniques have been employed in order to investigate the fluidized bed behavior: measurement of bed expansion, settling velocity, local reflectance (only for the microparticles), and laser-based planar imaging of the agglomerates (only for nanoparticles) have been carried out. Part of the experiments have been performed in different setups by different research groups in order to seek for reproducibility.

A main result derived from these experiments is that the size of agglomerates in fluidization does not depend essentially on the type of gas used at ambient conditions as theoretically expected. On the other hand, it is seen that an increment of gas viscosity enhances bed expansion and delays the onset of bubbling, which is attributable to a decrease on the size of small gas bubbles in the uniform fluid-like regime. These small bubbles are present in the nonbubbling fluid-like regime, and have been detected by local reflectance measurements.

For the micronsized particles, the fluidized bed is seen to transit from uniform fluidlike fluidization to bubbling. In the absence of visible large bubbles the bed expands according to the Richardson-Zaki equation, modified to take into account particle agglomeration. As the superficial gas velocity is increased, the frequency of small bubbles increases up to the onset of bubbling. At this point small bubbles coalesce into visible bubbles and bed expansion saturates.

The transition to a bubbling regime is rationalized from the estimation of the size of gas bubbles using the empirical Harrison criterion modified for agglomerates. From the Wallis criterion adapted to the fluidization of agglomerates, it is predicted that bubbling would occur at values of the particle volume fraction ϕ close to the experimentally measured ones. Using both criteria, it is predicted that bubbling should be fully suppressed, i.e., the gas-fluidized bed would transit directly from uniform fluidization to elutriation, in the limit of a high-viscosity gas ($\mu \gtrsim 4 \times 10^{-5}$ Pa s), whereas the window of uniform fluidization should shrink to zero in the limit of small viscosity ($\mu \lesssim 1 \times 10^{-5}$ Pa s).

As with respect to the nanoparticle systems, a transition from uniform fluidization to elutriation with full suppression of bubbling has been observed in beds of silica nanoparticles fluidized by nitrogen and neon. For this system the bed expands continuously as the gas velocity is increased, while the amount of elutriated particles increases, without saturation. This is expected from the empirical Harrison criterion adapted to fluidization of nanoparticle agglomerates, from which it is estimated that the size of the small bubbles in uniform fluidization is of the order or smaller than agglomerate size. Accordingly, the Wallis criterion adapted to fluidization of agglomerates predicts the absence of a bubbling regime. Concerning gas-fluidization of denser and larger nanoparticles (titania), we have observed a transition to bubbling fluidization, which is delayed by the use of the higher viscosity neon. Uniform fluidization for this system is, however, compromised by the use of a shallow bed. The fittings of bed expansion data to the modified Richardson-Zaki equa-

tion and laser based planar imaging allows us to estimate average agglomerate sizes of the order of hundred of microns, with a wide distribution and more or less independent of gas viscosity. Our work suggests that agglomerate size polydispersity could represent a relevant influence leading to stratification that is out of the scope of this article, but needs to be studied in the future.

Usually, granular systems fluidized by gas have shown a direct transition from solid to bubbling behavior. However, the particle size of these systems was of the order of 50 μm or larger, and, thus, particle agglomeration was negligible. In contrast, uniform fluidlike fluidization was the common behavior observed for beds fluidized by liquids. This has led many researchers to consider gas-fluidization as radically different from liquid-fluidization for many years.[22] For the fine and ultrafine powders studied in this work we have clearly identified a fluidlike regime characterized by the absence of visible gas bubbles, which is against an old misconception that gas-fluidized beds should always bubble. Not surprisingly, a simple calculation of the Froude number based on agglomerate size $Fr^* = v_g^2/(gd^{**})$ yield values on the order of 0.1 or smaller as for liquid-fluidized beds, and are representative of uniform fluidization behavior according to the pioneer work of Wilhelm and Kwauk.[3]

Acknowledgments

The Seville group acknowledges the Xerox Foundation, Spanish Ministerio de Ciencia y Tecnologia (contract FIS2006-03645) and Junta de Andalucia (contract FQM 421). The NJIT group gratefully acknowledges the National Science Foundation for financial support through Award #0210400, NIRT-Collaborative Research: Experimental and Computational Investigations of Fluid Interactions and Transport in Nanodomains and around Nanoparticles. We also thank Dr. Herbert Riemenschneider of the Degussa Corporation for supplying the nanoparticles used in the experiments.

Notation

A = Hamaker constant
A_i = area of an agglomerate as measured by laser based planar imaging
APF = agglomerate particulate fluidization
Bo_g = ratio of interparticle attractive force to particle weight
Bo_g^* = ratio of attractive force between simple-agglomerates to simple-agglomerate weight
d_a = typical size of particle surface asperities
d_i = individual agglomerate size as measured by laser based planar imaging
d^{NL} = number-length average diameter of the agglomerate
d^{SV} = surface-volume average diameter of the agglomerate
d^* = simple-agglomerate size
d^{**} = complex-agglomerate size
D = fractal dimension of the simple-agglomerate
D_a = global fractal dimension of the complex-agglomerate
D^* = fractal dimension of the complex-agglomerate
D_b = largest stable size of isolated fluid bubbles
f = average number of small gas bubbles per unit time detected by the optical probe
F_0 = interparticle attractive force
F_0^* = attractive force between simple-agglomerates
Fr = Froude number
Fr^* = Froude number based on agglomerate size
g = gravity acceleration
h = bed height
k_i = ratio of simple-agglomerate size to primary particle size
k^* = ratio of complex-agglomerate size to simple-agglomerate size
k^{**} = ratio of complex-agglomerate size to primary nanoparticle size
n = Richardson Zaki exponent
N = number of primary particles in a simple-agglomerate
N^* = number of simple-agglomerates in the complex-agglomerate
N^{**} = number of primary nanoparticles in the complex-agglomerate
p = particle-phase pressure
R = backscattered light intensity collected by an optical probe (reflectance)
Re = particle Reynolds number
U_b = rising velocity of isolated fluid bubbles
u_e = elastic wave velocity
u_e^* = elastic wave velocity for the fluidized bed of simple-agglomerates
u_e^{**} = elastic wave velocity for the fluidized bed of complex-agglomerates
u_ϕ = propagation velocity of a voidage disturbance
u_ϕ^* = propagation velocity of a voidage disturbance for the fluidized bed of simple-agglomerates
u_ϕ^{**} = propagation velocity of a voidage disturbance for the fluidized bed of complex-agglomerates
v_b = superficial gas velocity at the onset of bubbling
v_g = superficial gas velocity
v_J = gas velocity at the boundary between solidlike and fluidlike fluidization
v_{p0} = terminal settling velocity of the individual primary particles
v_s = initial settling velocity of the fluidized-bed free surface
v^* = terminal settling velocity of an individual simple-agglomerate
v^{**} = terminal settling velocity of an individual complex-agglomerate
W_p = particle weight
z_0 = distance of closest approach between two molecules

Greek letters

$\Delta v_g = v_{mb} - v_J$
ϕ = particle volume fraction
ϕ_b = particle volume fraction at the bubbling onset
ϕ_J = particle volume fraction at the boundary between solidlike and fluidlike fluidization
ϕ^* = volume fraction of simple-agglomerates
ϕ^{**} = volume fraction of complex-agglomerates
μ = gas viscosity
ρ_f = fluid density
ρ_g = particle density
ρ^* = simple-agglomerate density
σ = standard deviation of the reflectance

Literature Cited

1. Kruis FH, Fissan H, Peled A. Synthesis of nanoparticles in the gas phase for electronic, optical and magnetic applications-a review. *J Aerosol Sci.* 1998;29:511–535.
2. Nase ST, Vargas WL, Abatan AA, McCarthy JJ. Discrete characterization tools for cohesive granular material. *Powder Technol.* 2001; 116:214–223.
3. Wilhelm RH, Kwauk M. Fluidization of solid particles. *Chem Eng Prog.* 1948;44:201–218.
4. Kwauk M, Li J, Liu D. Particulate and aggregative fluidization 50 years in retrospect. *Powder Technol.* 2000;111:3–18.
5. Harrison D, Davidson JF, de Kock JW. On the nature of aggregative and particulate fluidisation. *Trans Inst Chem Eng.* 1961;39:202–211.
6. Davidson JF, Harrison D, Guedes de Carvalho JRF, Liquidlike behavior of fluidized bed. *Ann Rev Fluid Mech.* 1977;9:55–86.
7. Hoffmann AC, Yates JG. Experimental observations of fluidized beds at elevated pressures. *Chem Eng Commun.* 1986;41:133–149.
8. Clift R, Grace J.R. Mechanism of bubble break-up in fluidized-beds. *Chem Eng Sci.* 1972;27:2309–2310.
9. Duru P, Guazzelli E. Experimental investigation of the secondary instability of liquid-fluidized beds and the formation of bubbles. *J Fluid Mech.* 2002;470:359–382.
10. Clift R, Grace JR, Weber ME. Stability of bubbles in fluidized bed. *Ind Eng Chem Fundam.* 1974;13:45–51.
11. Jackson R. *The dynamics of fluidized particles.* Cambridge: Cambridge University Press, 2000.

12. Horio M, Nonaka A. A generalized bubble diameter correlation for gas-solid fluidized beds. *AICHE J*. 1987;33:1865–1872.
13. Wallis GB. *One Dimensional Two-phase Flow*. New York: McGraw-Hill, 1969.
14. Batchelor GK. A new theory on the instability of a uniform fluidized bed. *J. Fluid Mech.* 1988;193:75–110.
15. Batchelor GK. Sedimentation in a dilute polydisperse system of interacting spheres. Part I. General Theory. *J Fluid Mech.* 1982;119: 379–408. Batchelor GK Wen CS. Sedimentation in a dilute polydisperse system of interacting spheres. Part II. Numerical results. *J Fluid Mech.* 1982;124:495–528.
16. Sundaresan S. Instabilities in fluidized beds. *Annu Rev Fluid Mech.* 2003;35:63–88.
17. Zenit R, Hunt ML, Brennen CE, Collisional particle pressure measurements in solid-liquid flows. *J Fluid Mech.* 1997;353:261–283.
18. Guazzelli E. Fluidized Beds: from waves to bubbles. In: Hinrichsen H, Wolf DE. *The Physics of Granular Media*. Berlin: Wiley-VCH, 2004:213.
19. Foscolo PU, Gibilaro LG. A fully predictive criterion for the transition between particulate and aggregate fluidization. *Chem Eng Sci*. 1984;39:1667–1675.
20. Foscolo PU, Gibilaro LG. Fluid dynamic stability of fluidised suspensions: the particle bed model *Chem Eng Sci*. 1987;42:1489–1500. Gibilaro LG, Di Felice R, Foscolo PU. On the minimum bubbling voidage and the geldart classification for gas-fluidised beds. *Powder-Technol*. 1988;56:21–29. Rapagna S, Foscolo PU, Gibilaro LG. The influence of temperature on the quality of fluidization. *Int J Multiphase Flow*. 1994;20:305–313. Lettieri P, Brandani S, Yates JG, Newton D. A generalization of the Foscolo and Gibilaro particle-bed model to predict the fluid bed stability of some fresh FCC catalysts at elevated temperatures. *Chem Eng Sci*. 2001;56:5401–5412.
21. Glasser BJ, Kevrekidis IG, Sundaresan S. Fully developed travelling wave solutions and bubble formation in fluidized beds. *J Fluid Mech.* 1997;334:157–188.
22. Homsy GM. Nonlinear waves and the original of bubbles in fluidized beds. *Appl Sci Res.* 1998;58:251–274.
23. Valverde JM, Castellanos A. Types of gas fluidization of cohesive granular materials. *Phys Rev E*. 2007;75:031306(1–6).
24. Geldart D. Types of gas fluidization. *Powder Technol.* 1973;7:285–293.
25. Rietema K. The Dynamics of Fine Powders. London: Elsevier, 1991.
26. Richardson J.F. Incipient fluidization and particulate systems. In: Davidson JF, Harrison D. *Fluidization*. London: Academic Press, 1971:26–64.
27. Chaouki J, Chavarie C, Klvana D, Pajonk G. Effect of Interparticle forces on the hydrodynamic behavior of fluidized aerogels. *Powder Technol*. 1985;43:117–125.
28. Brooks EF, Fitzgerald TJ. Fluidization of novel dendrillar carbonaceous materials. In: Ostergaard K, Sorensen A. *Fluidization*. New York: Engineering Foundation, 1986:217–224.
29. Morooka S, Kusakabe K, Kobata A, Kato Y. Fluidization state of ultrafine powders. *J Chem Eng Jpn*. 1988;21:41–46.
30. Pacek AW, Nienow AW. Fluidisation of fine and very dense hardmetal powders. *Powder Technol*. 1990;60:145–158.
31. Valverde JM, Castellanos A, Mills P, Quintanilla MAS. Effect of particle size and inter-particle force on the fluidization behavior of gas-fluidized beds. *Phys. Rev. E*. 2003;67:051305(1–6).
32. Yang J, Sliva A, Banejee A, Dave RN, Pfeffer R. Dry particle coating for improving the flowability of cohesive powders. *Powder Technol*. 2005;158:21–33.
33. Castellanos A, Valverde JM, Quintanilla MAS. Physics of compaction of fine powders. *Phys Rev Lett*. 2005;94:075501(1–4).
34. Zhu C, Yu Q, Dave RN, Pfeffer R. Gas fluidization characteristics of nanoparticle agglomerates. *AIChE J*. 2005;51:426–439.
35. Valverde JM, Quintanilla MAS, Castellanos A, Mills P. The settling of fine cohesive powders. *Europhys Lett*. 2001;54:329–334.
36. Castellanos A, Valverde JM, Quintanilla MAS. Aggregation and sedimentation in gas-fluidized beds of cohesive powders. *Phys. Rev E*. 2001;64:041304(1–7).
37. Witten TA, Sander LM. Diffusion-limited aggregation, a kinetic critical phenomenon. *Phys Rev Lett*. 1981;47:1400–1403.
38. Castellanos A. The relationship between attractive interparticle forces and bulk behaviour in dry and uncharged fine powder. *Adv Phys*. 2005; 54:263–376.
39. Yao W, Guangsheng G, Fei W, Wu J. Fluidization and agglomerate structure of SiO_2 nanoparticles. *Powder Technol*. 2002;124:152–159.
40. Valverde JM, Castellanos A. Fluidization of nanoparticles: A modified Richardson-Zaki law. *AIChE J*. 2006;52:838–842.
41. Nam C, Pfeffer R, Dave RN, Sundaresan S. Aerated vibrofluidization of silica nanoparticles. *AIChE J*. 2004;50:1776–1785.
42. Valverde JM, Castellanos A. High viscosity gas fluidization of fine particles: an extended window of quasihomogeneous flow. *Phys Rev E*. 2006;74:021302(1–6).
43. Valverde JM, Quintanilla MAS, Castellanos A, Mills P. Experimental study on the dynamics of gas-fluidized beds. *Phys Rev E*. 2003; 67:016303(1–5).
44. Johnsson F, Zijerveld RC, Schouten JC, van den Bleek CM, Leckner B. Characterization of fluidization regimes by time-series analysis of pressure fluctuations. *Int. J of Multiphase Flow*. 2000;26:663–715.
45. Valverde JM, Castellanos A, Quintanilla MAS. The memory of granular materials. *Contemp. Phys*. 2003;44:389–399.
46. ImageJ 1.29× Wayne Rasband, National Institute of Health, USA, http://rsb.info.nih.gov/ij/
47. Piepers HW, Cottaar EJE, Verkooijen AHM, Rietema K. Effects of pressure and type of gas on particle–particle interaction and the consequences for gas-solid fluidization behaviour. *Powder Technol*. 1984;37:55–70.
48. Krupp H. Particle adhesion-theory and experiment. *Adv Coll Inter Sci*. 1967;1:111–239.
49. Zhu C, Liu G, Yu Q, Pfeffer R, Dave R, Nam C. Sound assisted fluidization of nanoparticle agglomerates. *Powder Technol*. 2004;141: 119–123.
50. Wang XS, Palero V, Soria J, Rhodes MJ. Laser-based planar imaging of nano-particle fluidization: Part II - mechanistic analysis of nanoparticle aggregation. *Chem Eng Sci*. 2006;61:8040–8049.
51. Wang XS, Palero V, Soria J, Rhodes MJ, Laser-based planar imaging of nano-particle fluidization: Part I - determination of agglomerate size and shape. *Chem Eng Sci*. 2006;61:5476–5486.
52. Valverde JM, Castellanos A. Effect of vibration on agglomerate particulate fluidization. *AIChE J*. 2006;52:1705–1714.

Manuscript received Jan. 10, 2007, revision received Jun. 29, 2007, and final revision recieved Sept. 10, 2007.